

Surface wind and vertical extent features of the explosive cyclones in the Northern Hemisphere based on the ERA-I reanalysis data

Li-Zhi Jiang^{1,2,3}  | Shen-Ming Fu⁴  | Jian-Hua Sun¹ | Rui Fu⁵ | Wan-Li Li⁶ | Si-Xiong Zhao⁴ | Hui Wang⁷

¹Key Laboratory of Cloud-Precipitation Physics and Severe Storms, Institute of Atmospheric Physics, Chinese Academy of Sciences, Beijing, China

²College of Earth and Planetary Sciences, University of Chinese Academy of Sciences, Beijing, China

³Fujian Key Laboratory of Severe Weather, Fujian Institute of Meteorological Sciences, Fujian, China

⁴International Center for Climate and Environment Sciences, Institute of Atmospheric Physics, Chinese Academy of Sciences, Beijing, China

⁵Yunnan Research Institute of Meteorology, Yunnan Meteorological Bureau, Kunming, China

⁶China Meteorological Administration Training Center, Beijing, China

⁷National Meteorological Center, Beijing, China

Correspondence

Shen-Ming Fu, International Center for Climate and Environment Sciences, Institute of Atmospheric Physics, Chinese Academy of Sciences, Beijing 100029, China.

Email: fusm@mail.iap.ac.cn

Funding information

National Key R&D Program of China, Grant/Award Number: 2018YFC0809400; National Natural Science Foundation of China, Grant/Award Numbers: 41775046, 42075002; the Youth Innovation Promotion Association, Chinese Academy of Sciences; the National Key Scientific and Technological Infrastructure project “Earth System Science Numerical Simulator Facility”

Abstract

Although explosive cyclones (ECs) have long been a focus of research, there remains a lack of knowledge of the statistical characteristics of their associated maximum surface winds and vertical extents. This study fills this gap by conducting a targeted statistical analysis of ECs in the Northern Hemisphere using the ERA-I reanalysis data during a 40-year period. Some new findings are obtained: (a) The average location of formation of ECs undergoes a notable westward and equatorward shift from September to April in the next year which is consistent with the location variations of sea surface temperature's strong gradients in subtropical regions. (b) Extreme ECs with a deepening rate more than 2.0 Bergeron or with a longer lifespan more than 10 days tend to have a larger occurrence number over the Northern Atlantic Ocean than over the Northern Pacific. (c) The maximum surface wind associated with an EC tends to appear between the EC reaching its maximum deepening rate and reaching its minimum central pressure. (d) The northeastern quadrant of ECs accounts for the highest proportion of maximum surface wind and strongest wind speed, as the baroclinic energy conversion is generally strongest in this quadrant. (e) Over 60% of ECs belong to a type of vertically deep cyclone (ECs' top levels show close relationship to ascending motions within their central regions), and they tend to reach their maximum vertical extent around the time when they reach their minimum central pressures. (f) The highest top levels of ECs exhibit an overall upward extending trend as their minimum central pressure decreases or their maximum deepening rate increases.

KEY WORDS

explosive cyclones, maximum surface winds, vertical extent of cyclones

1 | INTRODUCTION

Over the oceans in middle and high latitudes, a special type of cyclone often appears, called an “explosive cyclone (EC)” because it exhibits a large deepening rate. Sanders and Gyakum (1980) developed a quantitative standard for defining this type of cyclone: over a 24-hr period, if the deepening rate of the central sea level pressure (SLP) of a cyclone exceeds 1 hPa h^{-1} (relative to the equivalent latitude of 60°N), the cyclone is an EC. During its stage of rapid development, an EC can induce cold waves, billows and blizzards, all of which have tremendous destructive power. Consequently, this type of cyclone has long been a research focus for meteorologists (e.g., Sanders and Gyakum, 1980; Bosart, 1981; Uccellini *et al.*, 1985; Sanders, 1987; Jia and Zhao, 1994; Davis *et al.*, 1996; Browning, 2004; Yoshida and Asuma, 2004; Lagouvardos *et al.*, 2007; Kuwano-Yoshida and Asuma, 2008; Kouroutzoglou *et al.*, 2011a, 2011b; Yamamoto, 2012; Fu *et al.*, 2014; Hirata *et al.*, 2015; Fu *et al.*, 2018; Schultz *et al.*, 2018; Brâncuș *et al.*, 2019; Fu *et al.*, 2020). Strong winds are another important type of disastrous weather that are caused by ECs. Based on case studies, Browning (2004) and Brâncuș *et al.* (2019) found that strong winds could appear equatorward of the cyclone's centre. However, whether the regions equatorward of ECs' centres possess the largest proportion of strong winds still needs a further investigation. Warm conveyer belts were often found to be accompanied with ECs (Binder *et al.*, 2016). They play an unnegelectable role in the development of ECs, particularly for its precipitation (Catto *et al.*, 2015) and severe winds (Martínez-Alvarado *et al.*, 2014; Binder *et al.*, 2016; Brâncuș *et al.*, 2019).

The climatological and statistical characteristics of ECs are a key area of research. In early studies, synoptic charts were used to analyse the climatological characteristics. It was found that most ECs formed over the western coasts of the Pacific and Atlantic Oceans during the wintertime (Sanders and Gyakum, 1980; Murty *et al.*, 1983; Roebber, 1984; Chen *et al.*, 1992; Ding *et al.*, 1998). Benefiting from the development of observation technology, numerical models, and data assimilation systems, the performance of various types of reanalysis datasets has been greatly improved. This has made reanalysis of data an effective method for climatological/statistical and related studies of ECs. Correspondingly, many new results on this type of cyclone have been obtained. For example, Yoshida and Asuma (2004) applied a five-cold-season statistical analysis to ECs over the northwestern Pacific using the global objectively analysed dataset (GANAL). They found that favourable atmospheric conditions for intensification of ECs were closely related to the presence and extension of cold air masses over the Asian continent. Iwao

et al. (2012) showed that there was an increasing trend in the numbers of ECs over the northwest Pacific from 1979 to 2010 based on a manually verified objective tracking algorithm using the 6-hourly and $1.25^\circ \times 1.25^\circ$ JRA-25 reanalysis data. Zhang *et al.* (2017) used NCEP–FNL data to analyse ECs over the North Atlantic during a 15-cold-season period, and showed that ECs' occurrence frequency was highly correlated with the intensity of lower-level baroclinity. On the basis of a 34-extended-winter statistical analysis (from 1979 to 2012) using ERA-I reanalysis data, Hart *et al.* (2017) found that ECs were a main cause of cyclone-related strong wind events over the British Isles.

A cyclone is a three-dimensional system (Kouroutzoglou *et al.*, 2012; Jiang *et al.*, 2020), and thus it has a vertical extent, within which each level has a remarkable closed cyclone centre belonged to the same cyclone (Li *et al.*, 2019). The vertical extent of a cyclone is closely related to its evolution. As mentioned above, previous climatological/statistical studies of ECs have shown many key characteristics of this type of cyclone. However, the fundamental features related to ECs' vertical extent still remain poorly understood. Although a few previous studies (e.g., Rossa *et al.*, 2000; Novak *et al.*, 2010; Campins *et al.*, 2011; Čampa and Wernli, 2012; Binder *et al.*, 2016; Pang and Fu, 2017) have discussed cyclones' vertical structures, they did not directly focus on the closed cyclone centres at different vertical levels, instead, they used positive PV and/or cyclonic vorticity as an alternative. This would introduce errors into the analysis, as positive PV and/or cyclonic vorticity centres are not equivalent to real cyclones (Flocas *et al.*, 2010; Fu *et al.*, 2016, 2020), which would result in a notable false alarm rate (Colle *et al.*, 2013). Moreover, in many situations, the closed cyclone centre shows a notable distance to the centres of PV and cyclonic vorticity (Fu *et al.*, 2015). Therefore, one primary purpose of this study is to fill the research gap by focusing on features related to the vertical extent of ECs in the Northern Hemisphere. In addition, although severe winds associated with ECs are among the most important disastrous weather phenomena (Browning, 2004; Parton *et al.*, 2010; Hewson and Neu, 2015; Hart *et al.*, 2017; Brâncuș *et al.*, 2019), the key statistical features of these winds still remain vague. Therefore, this study also conducts a statistical analysis on the maximum surface winds associated with ECs.

The remainder of the paper is organised as follows: the data, methods, and cyclone parameters used in this study are described in Section 2, classical features of ECs are presented in Section 3, new findings on the EC-associated maximum surface winds and on their vertical extent are provided in Section 4, and finally a conclusion and discussion are presented in Section 5.

2 | DATA, METHODS, AND CYCLONE PARAMETERS

2.1 | Data

A comparison on the climatology of ECs using NCEP, JRA25, ERA40, and ERA-I reanalysis datasets indicates that a higher-resolution reanalysis dataset has more advantages in investigating ECs than those of lower-resolution (Allen *et al.*, 2010; Kouroutzoglou *et al.*, 2011b, 2013) since the former has a better performance in the identification of smaller scale and/or transitioning systems. This study uses the 6-hourly $0.75^\circ \times 0.75^\circ$ ERA-I reanalysis data (<https://doi.org/10.5065/D6CR5RD9>) from the European Centre for Medium-Range Weather Forecasts (ECMWF, 2009) for detecting ECs during the period of 1979–2018 and the associated analyses. This dataset is of higher horizontal resolution than most datasets used in previous statistical studies. ERA-I has good performance in representing ECs and other synoptic scale systems (Tilinina *et al.*, 2013; Rudeva and Simmonds, 2015; Hart *et al.*, 2017; Fu *et al.*, 2020; Pepler and Dowdy, 2020). It should be noted that although more advanced data sets such as ERA5 are available recently, ERA-I is sufficient to describe the synoptic scale (or larger scale) features of ECs. The Sea level pressure (SLP) and geopotential height at the pressure levels from 1,000 to 200 hPa are used to identify ECs. Similar to the region used in Ding *et al.* (1998), Allen *et al.* (2010), and Zhang *et al.* (2017), we focus only on the ECs that form in the Northern Hemisphere within the range of 25° – 80°N , 0° – 360° . In order to exclude tropical cyclones, all ECs identified in this study were confirmed to form north of 25°N (i.e., they are not generated in tropical regions) and have intense lower-level temperature gradients (i.e., their baroclinity was strong).

2.2 | Detection methods and cyclone parameters

2.2.1 | Cyclone detection

Identifying cyclones correctly is important to this study. We use the eight-section slope-detecting method (ESSD method) developed by Jiang *et al.* (2020) in this study. The ESSD method uses a restrictive criteria that gradient in all eight directions should be higher than a certain threshold, which has been proven to be effective and accurate (according to their random test, this method can render a mean detection accurate rate of $\sim 85\%$, better than the mean detection accurate of $\sim 80\%$ of traditional local minimum

pressure method) in detecting extratropical cyclones by using reanalysis data of relatively high resolution. The parameters used in this method are presented in Table 1. In the pressure coordinate, within a cyclone's vertical extent, the level of maximum/minimum pressure is defined as its bottom/top level. For the bottom level of a cyclone, the detection is conducted using SLP (Sinclair, 1994; Grigoriev *et al.*, 2000; Allen *et al.*, 2010; Ulbrich *et al.*, 2013; Zhang *et al.*, 2017). For the levels above the bottom, geopotential height is used to determine the closed cyclone centre (Lim and Simmonds, 2007; Fu and Sun, 2012; Li *et al.*, 2019). All detected cyclones in this study are verified manually to guarantee that they are real extratropical cyclones.

2.2.2 | Determination of vertical extent

After a cyclone has been detected using SLP, geopotential height is used to determine its vertical extent, that is, the vertical distance between its bottom (in this study, we use SLP) and top levels. Usually, the height of a same pressure level is lower at the higher latitudes than that in the lower latitudes. Therefore, at different latitudes, lower top-level pressure does not always mean higher height. The procedure consists mainly of two steps: (a) detecting all closed cyclone centres (by using the ESSD method) at different vertical levels using the geopotential-height data within a circle centred at the centre of the surface EC and of radius 2,300 km. This radius has been tested to show the best performance for our tracking algorithm, as it is big enough to consider a tracked EC's vertical tilting and meanwhile small enough to exclude the ECs (as many as possible) other than the tracked one. (b) determining which closed cyclone centres belong to the same cyclone (that is first determined using SLP). For the first step, we again use the eight-section slope-detecting method to detect cyclones (the parameters are shown in Table 1). For the second step, two criteria are used to ensure that the closed cyclone centres at two neighbouring levels belong to the same cyclone: (a) the detected cyclones at these two neighbouring levels must have a similarity exceeding 60%. The similarity is determined by calculating the correlation coefficient between the geopotential height fields at two levels (i.e., field correlation). The calculation is conducted within two circles of the same radius of 500 km (which is tested to show a good performance for representing the central region of an EC). These two circles are at neighbouring vertical levels with their centres centred at the ECs' centre at their respective levels. (b) The horizontal distance between the two closed cyclone centres (the interval between vertical levels is 25 hPa in this study) must be less than 250 km.

TABLE 1 Procedures and objectives during cyclone detection

Procedures	Objectives
A 13×13 point smoothing is conducted on both SLP and geopotential height	To remove noise (Sinclair, 1994) and to increase the accuracy and stability of the detection method
The threshold value of the relative slope of SLP is 0.3	To ensure accuracy of the ESSD method in detecting cyclones using SLP
The total box size for detecting cyclones by using SLP is $9^\circ \times 9^\circ$	The same as above
In the SLP field, $\geq 1/3$ of the grid points covered by a cyclone must have an altitude below 500 m	To remove the uncertainty in detecting cyclones using SLP that is caused by high terrain
The threshold value of the relative slope of geopotential height is 0.03	To ensure accuracy of the ESSD method in detecting cyclones using geopotential height
The sliding box size for detecting cyclones by using geopotential height is $12^\circ \times 12^\circ$	The same as above

2.2.3 | Tracking algorithm

This study tracks a cyclone using only its bottom level, which is based on SLP. The main procedures are as follows. The ERA-I data are linearly interpolated from a temporal resolution of 6-hourly to 3-hourly. The cyclone centres are detected 3 hr after the current time, and the nearest cyclone centre to the current cyclone centre is found. (a) If the distance between the two cyclone centres is less than 700 km and (b) the two cyclones are similar to each other (i.e., their field-correlation exceeds 60%), then the two cyclones are regarded as the same cyclone (the calculation is conducted within two circles of the same radius of 500 km. These two circles are at neighbouring time steps with their centres centred at the ECs' centre at their respective levels. Otherwise, if condition (a) is not satisfied, the tracking is terminated. If only condition (b) is not met, we use the second-nearest cyclone centre and judge whether this cyclone can satisfy both conditions (a) and (b). This loop goes on until the cyclone has been found 3 hr after the current time or the tracking is terminated. All cyclones detected using the automatic algorithm are checked manually since merging and splitting may introduce errors in the detection result. We use the following method to validate the tracking results: (a) when merging of several cyclones occurs, the merged cyclone is considered to be the continuation of the previous largest cyclone; (b) when a cyclone splits into several cyclones, the largest cyclone after splitting is considered to be the continuation of the original cyclone. ECs' average track is calculated using the trajectory clustering method developed by Lee *et al.* (2007).

2.2.4 | Cyclone parameters

Sanders and Gyakum (1980) first defined the deepening rate of an EC as the change in its central SLP during a 24-hr period at an equivalent latitude of 60°N . Simmonds and Wu (1993) used the relative central SLP (i.e., cyclone's central SLP minus the relevant monthly mean SLP) to calculate the deepening rate. Yoshida and Asuma (2004) developed a similar definition to that of Sanders and Gyakum (1980), but used a 12-hr period for calculation. This definition has a higher temporal resolution than that of Sanders and Gyakum (1980), and it therefore gives a calculated deepening rate which is much closer to the real situation. In this study, we have adopted Yoshida and Asuma's definition to calculate the deepening rate as follows:

$$\text{DR} = \left[\frac{p(t-6) - p(t+6)}{12} \right] \left[\frac{\sin 60^\circ}{\sin \frac{\phi(t-6) + \phi(t+6)}{2}} \right], \text{ where } t \text{ is time (hr), } p \text{ is}$$

the cyclone's central SLP (hPa), and ϕ is the latitude of the cyclone centre.

In this study, a detected extratropical cyclone will be regarded as an EC if it satisfies all of the following three criteria: (a) it must last for at least 24 hr (short-lived cyclones are not considered in this study); (b) its minimum central pressure must be less than 1,000 hPa (relatively weak cyclones are not considered); (c) its maximum deepening rate must be ≥ 1 Bergeron (Yoshida and Asuma, 2004). Seven typical stages of an EC are defined: (a) cyclone formation time (CFT), (b) first explosive-development time (FET), (c) maximum deepening time (MDT), (d) highest top-level time (HTT), (e) maximum surface (at the height of 10 m) wind speed time (MST), (f) minimum pressure time (MPT), and (g) last detection time

(LDT). The above seven typical stages correspond respectively to (a) the time when an EC's centre is first detected, (b) the time when the EC first reaches the explosive development criterion (i.e., a deepening rate ≥ 1 Bergeron), (c) the time when the EC's deepening rate reaches its maximum, (d) the time when the EC reaches its highest top level (it is also the time when an EC reaches its largest vertical extent), (e) the time when the EC gains its maximum surface wind speed, (f) the time when the EC's central SLP reaches its minimum, and (g) the time when the EC is detected for the last time. Similar to Messmer and Simmonds (2021), the maximum surface wind speed associated with an EC is the maximum surface wind speed that appears during its whole lifespan within a range that is centred on the EC's centre and has a radius of 2000 km (usually, an EC can affect such an area, and the results are insensitive to $\pm 10\%$ changes to this radius).

The baroclinic energy conversion (BEC; $BEC = -\alpha\omega$, where α is specific volume, and ω is vertical velocity in pressure coordinate), which indicates the conversion between available potential energy (APE) and kinetic energy (KE) (Lorenz, 1955; Murakami, 2011) is calculated to explain the features of maximum surface winds associated with ECs.

2.2.5 | Significance test and Lagrange composite

In this study, the “*t* test” (Devore, 2004) is used to test the significance level of (a) the proportion differences between two types of ECs, and (b) the linear correlation. The Whitney “*U* test” (Mann and Whitney, 1947; Pepler and Dowdy, 2020) is used to test the significance levels of the differences between the mean values (e.g., frequencies, lifespans, deepening rates, winds) of different types of ECs. If the significance test can pass the level of 0.1 (i.e., $p < 0.1$, where p is the probability of obtaining test results at least as extreme as the results actually observed, under the assumption that the null hypothesis is correct.) or a smaller value (e.g., 0.05, 0.01), we consider it is statistically significant, otherwise it is not statistically significant. Lagrange composite of ECs are conducted in this study: (a) the coordinate origin is the centres of ECs, and (b) the range for composite is a box centred in the coordinate origin which has an area of 30 latitudes \times 30 longitudes. This range is big enough to include ECs' main body.

3 | CLASSICAL STATISTICAL CHARACTERISTICS

After manual verification, a total of 2078 ECs are identified in the Northern Hemisphere during the 40-year

study period (Table 2). Of these, apart from $\sim 0.43\%$ that occur in the Mediterranean and western Siberia, most ECs appear over the Pacific, Atlantic, and Arctic Oceans (Figures 1 and 2). According to this, ECs in the Northern Hemisphere are divided into two main categories, namely, the northern Pacific Ocean–Arctic Ocean type (PAT), which form within (25° – 80° N, 100° E– 120° W), and the northern Atlantic Ocean–Arctic Ocean type (AAT), which form within (25° – 80° N, 120° W– 30° E).

3.1 | Tracks and key features at typical stages

After formation, PAT and AAT ECs tend to move north-eastward (Figure 1), and get more concentrated in spatial range with time (Figure 2). In general, most PAT ECs tend to form around the Japan Sea (Figure 2a), begin explosive development and reach their most rapid deepening over the sea east of Japan (Figure 2b,c), gain minimum pressure around the middle northern Pacific Ocean (Figure 2d), and dissipate in regions west of Alaska (Figure 2e). Most AAT ECs tend to form around the junction of the Sargasso Sea and the North American continent (Figure 2a), enter their explosive development stage and reach their maximum deepening rate around Newfoundland (Figure 2b,c), reach their minimum pressure in regions southeast of Greenland (Figure 2d), and dissipate over the Greenland Sea (Figure 2e). On average, after formation, it takes ~ 22 hr for PAT ECs to enter their explosive development stage, ~ 29 hr to reach their maximum deepening rate, ~ 63 hr to reach their minimum pressure, and ~ 118 hr to dissipate (Table 3). For AAT ECs, it lasts for less time than the PAT ECs ($p < 0.01$). Compared to PAT, AAT needs less time to enter their FET (~ 21 hr), MDT (~ 26 hr), MPT (~ 59 hr), and LDT (~ 108 hr), and its mean deepening rate is larger. This means that AAT generally develop more rapidly than PAT. A Lagrange composite of the gradients of sea surface temperature (SST) (Figure 3), and a Lagrange composite of maximum Eady growth rate (EGR) (Figure 4) show that, overall, at different stages, the SST gradients and maximum EGR are stronger for AAT. This means that baroclinity is more intense for AAT, which contributes to its rapid development.

3.2 | Annual and monthly occurrence frequencies

ECs occur every year in the Northern Hemisphere, with the lowest occurrence frequency of 34 in 1979 and

TABLE 2 Monthly occurrence frequency and percentage of different types of ECs

Month	All		PAT		AAT	
	Frequency	Percentage	Frequency	Percentage	Frequency	Percentage
Jan	405	19.5%	195	17.6%	209	21.7%
Feb	350	16.8%	171	15.4%	179	18.6%
Mar	270	13.0%	165	14.9%	103	10.7%
Apr	118	5.7%	71	6.4%	45	4.7%
May	35	1.7%	26	2.3%	9	0.9%
Jun	6	0.3%	3	0.3%	3	0.3%
Jul	0	0.0%	0	0.0%	0	0.0%
Aug	2	0.1%	0	0.0%	2	0.2%
Sep	63	3.0%	30	2.7%	33	3.4%
Oct	173	8.3%	96	8.7%	76	7.9%
Nov	284	13.7%	156	14.1%	127	13.2%
Dec	372	17.9%	195	17.6%	175	18.2%
Total	2078	100.0%	1,108	100.0%	961	100.0%

Note: Values (in the fifth and seventh columns) in bold-italic, italic and bold mean that the differences between PAT and AAT pass the significance tests of levels 0.01, 0.05, and 0.1, respectively; whereas values in normal mean that the differences between PAT and AAT are not statistically significant.

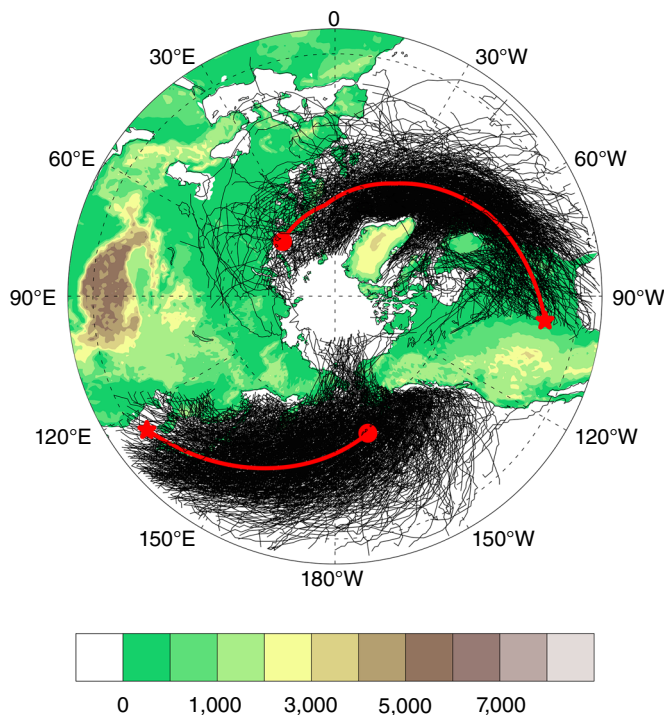


FIGURE 1 Explosive cyclone tracks over the period 1979–2018. The shaded area denotes the terrain height (unit: m). The red lines are the average paths of PATs and AATs, with the stars and circles indicating the average starting and ending locations, respectively [Colour figure can be viewed at wileyonlinelibrary.com]

the highest frequency of 69 in 2000 (Figure 5a). On average, ~52 ECs occur each year during the 40-year study period, which is ~7 larger than that found by Lim

and Simmonds (2002). The PAT ECs exhibit different features from the AAT ECs: the maximum and minimum annual occurrence numbers of AAT ECs are 34 (in 2007) and 11 (in 1979), respectively (Figure 5a), whereas for PAT ECs, these numbers are 45 (in 2000) and 17 (in 1989), respectively. Overall, ~28 PAT and ~24 AAT ECs occur every year. There are no significant linear trends for annual frequency series of PAT, AAT and their both.

A notable single-peak wave pattern is found in the monthly occurrence numbers of PAT, AAT, and their both (Table 2). Their peak values all occur in January (for PAT, another peak appears in December), and their minimum values all occur in July, when no ECs are detected. The average formation longitudes of all ECs and PAT tend to move westward from September to April in the next year ($p < 0.01$) (Figure 5b). The average latitudes of PAT ($p < 0.1$), AAT ($p < 0.05$) and their both ($p < 0.01$) tend to move equatorward during the same period (Figure 5c). The location variations of ECs' formation are consistent with the location variations of SST's strong gradients in subtropical regions over the North Pacific Ocean and the North Atlantic Ocean (not shown), both of which are closely related to annual cycle of the subtropical gyre. Seasonal variation is notable for ECs. Overall, ~54.2% of ECs form in winter (DJF), when their mean deepening rate reaches its maximum of ~1.3 Bergeron and their mean minimum central pressure reaches its lowest value of ~971 hPa.

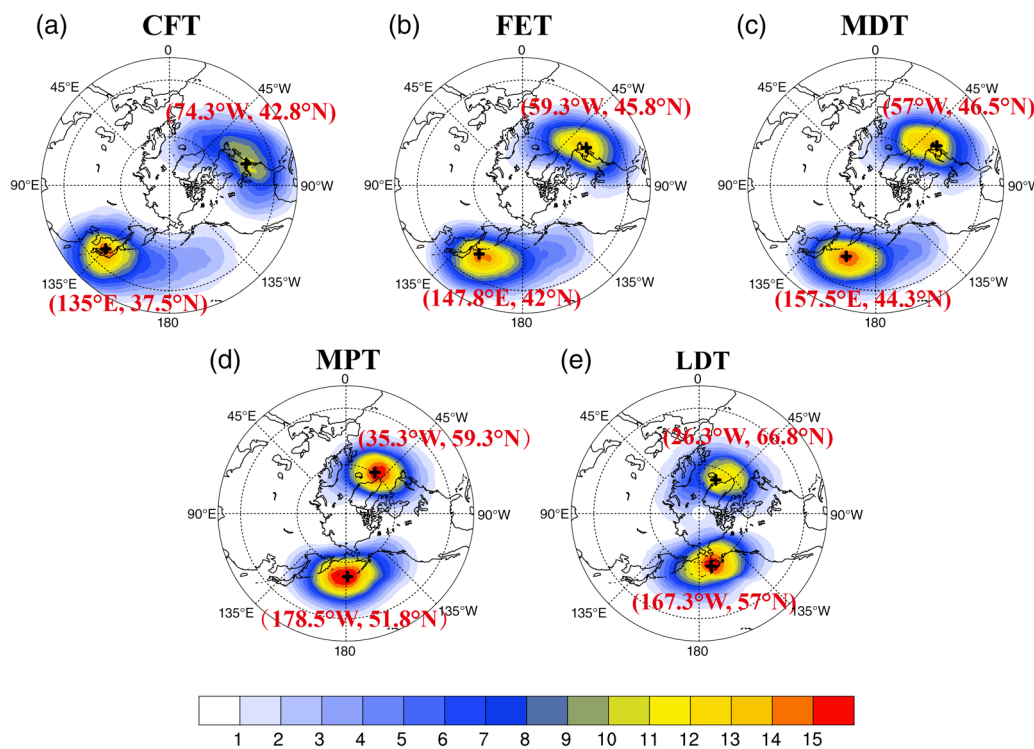


FIGURE 2 Spatial distribution of ECs (the shading represents their occurrence frequency) at five typical stages: (a) CFT; (b) FET; (c) MDT; (d) MPT; (e) LDT. The red text refers to the position of maximum-occurrence-frequency [Colour figure can be viewed at wileyonlinelibrary.com]

TABLE 3 All-event averaged time for different types of ECs to enter their different typical stages

Time (hr)	FET-CFT	MDT-CFT	MST-CFT	MPT-CFT	HTT-CFT	LDT-CFT
ALL	21.8	27.6	49.2	60.6	60.2	113.4
PAT	22.1	28.6	49.3	62.5	64.4	118.1
AAT	21.4	26.4	49.1	58.6	55.7	108.3

Note: For example, “FET-CFT” means from CFT to FET. Values (in the third and fourth lines) in bold-italic, italic and bold mean that the differences between PAT and AAT pass the significance tests of levels 0.01, 0.05, and 0.1, respectively.

Abbreviations: CFT, cyclone formation time; FET, first explosive-development time; MDT, maximum deepening time; MST, maximum surface wind speed time; MPT, minimum pressure time; HTT, highest top-level time; LDT, last detection time.

3.3 | Relationships between EC occurrence and lifespan

In the Northern Hemisphere, the occurrence frequency of ECs first increases as their lifespans lengthen, and then decreases with further increases in lifespan (Table 4). The ECs that mainly last for a lifespan of 48–168 hr (each EC group accounts for a percentage $\geq 10\%$) contributes to an accumulated proportion of $\sim 76\%$. These ECs mainly form in the western and middle sections of the Northern Pacific Ocean and the western section of Northern Atlantic Ocean (Figure 6b–f), with two high-frequency centres (>0.7) appearing around Japan and the junction of the Sargasso Sea and the North American continent. The EC groups with lifespans 72–96 hr and 96–120 hr account for the highest

proportion of $\sim 36.8\%$ (Table 4), whereas, the groups with lifespans 264–288 hr and ≥ 288 hr account for the lowest proportion ($<2\%$). These long-lived ECs tend to form around Japan and the eastern section of the North American continent (not shown).

The ECs over the two oceans show obvious differences: (a) Overall, PAT ECs have a larger occurrence number than AAT ECs (~ 1.2 times) (Table 4). This is true for the EC groups with lifetime 72–240 hr, whereas for other EC groups, AAT ECs have a larger occurrence number (~ 1.4 times that of PAT ECs). (b) In general, the mean lifespan of PAT ECs is longer than that of AAT ECs (Table 3); however, for extremely long-lived ECs that last for more than 10 days, the occurrence number of AAT ECs is ~ 1.7 times of that of PAT ECs (Table 4).

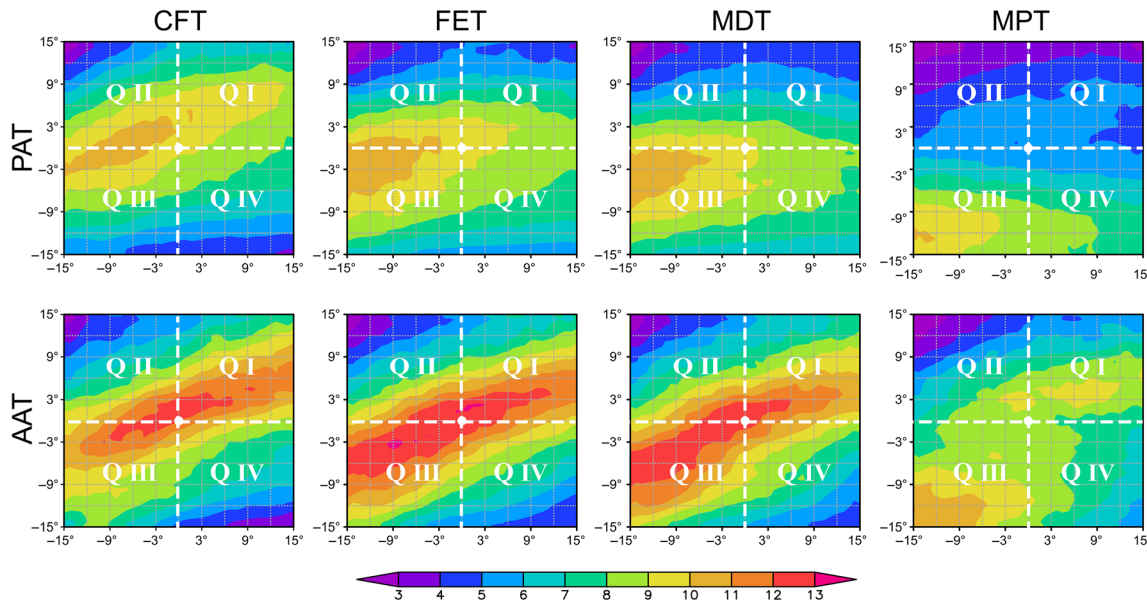


FIGURE 3 Composite (based on the Lagrange viewpoint) sea surface temperature gradient (shading, unit: $0.1 \text{ K } [100 \text{ km}]^{-1}$) of PAT and AAT at typical stages, where the big white dot shows ECs' centres, and the white dash lines mark the four quadrants: Q I, Q II, Q III, and Q IV [Colour figure can be viewed at wileyonlinelibrary.com]

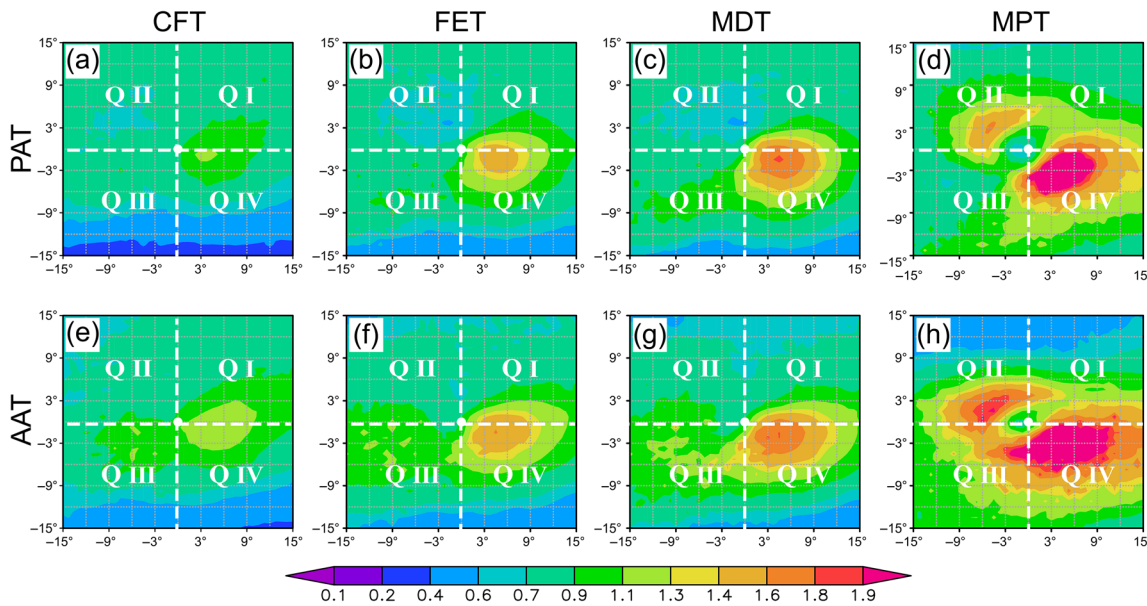


FIGURE 4 Composite (based on the Lagrange viewpoint) 900-hPa maximum Eady growth rate (shading, unit: day^{-1}) of PAT and AAT at typical stages, where the big white dot shows ECs' centres, and the white dash lines mark the four quadrants: Q I, Q II, Q III, and Q IV [Colour figure can be viewed at wileyonlinelibrary.com]

3.4 | Relationships between EC occurrence and maximum deepening rate

For PAT, AAT and their both, the occurrence frequencies mainly decrease as their deepening rates increase (Table 5). For weak ECs (i.e., those with a deepening rate of 1.0–1.3 Bergeron), their contribution is ~64%; for moderate ECs (1.3–1.7 Bergeron), they account for ~29.3%,

and for strong and super ECs (above 1.7 Bergeron), their proportion is ~6.7%. Weak PAT ECs have two maximum-occurrence-frequency centres (one located around the south of Japan and the other in the middle Northern Pacific Ocean), and weak AAT ECs have three maximum-occurrence-frequency centres (regions south of the Great Lakes of North America, south of Newfoundland, and southeast of Greenland) (Figure 7a). Moderate

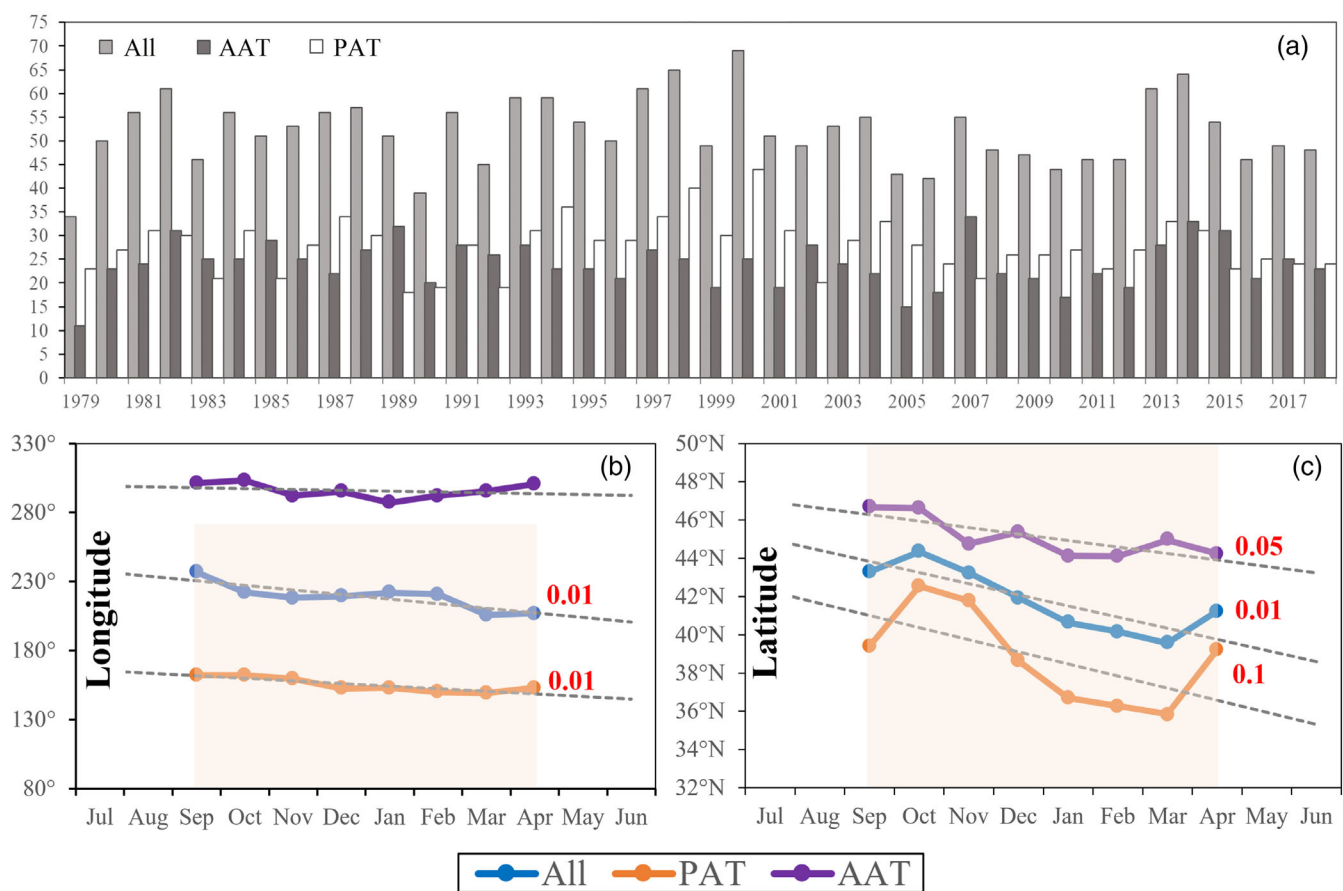


FIGURE 5 Annual occurrence frequencies of AAT, PAT, and both types of ECs in the Northern Hemisphere (a). The average formation longitudes for PAT, AAT, and their both, respectively (b), where shading marks those pass the significance test, with the red values showing the significance level. Panel (c) is the same as (b), but for average formation latitudes [Colour figure can be viewed at wileyonlinelibrary.com]

TABLE 4 Occurrence frequency and percentage of different types of ECs relative to their lifespans

Lifespan (hr)	All		PAT		AAT	
	Frequency	Percentage	Frequency	Percentage	Frequency	Percentage
24–48	176	8.5%	69	6.2%	106	11.0%
48–72	282	13.6%	125	11.3%	155	16.1%
72–96	392	18.9%	197	17.8%	192	20.0%
96–120	372	17.9%	206	18.6%	165	17.2%
120–144	321	15.4%	188	17.0%	133	13.8%
144–168	213	10.3%	136	12.3%	76	7.9%
168–192	143	6.9%	95	8.6%	47	4.9%
192–216	81	3.9%	49	4.4%	32	3.3%
216–240	46	2.2%	24	2.2%	22	2.3%
240–264	25	1.2%	9	0.8%	16	1.7%
264–288	15	0.7%	5	0.5%	10	1.0%
≥288	12	0.6%	5	0.5%	7	0.7%
Total	2078	100.0%	1,108	100.0%	961	100.0%

Note: Values (in the fifth and seventh columns) in bold-italic, italic and bold mean that the differences between PAT and AAT pass the significance tests of levels 0.01, 0.05, and 0.1, respectively; whereas values in normal mean that the differences between PAT and AAT are not statistically significant.

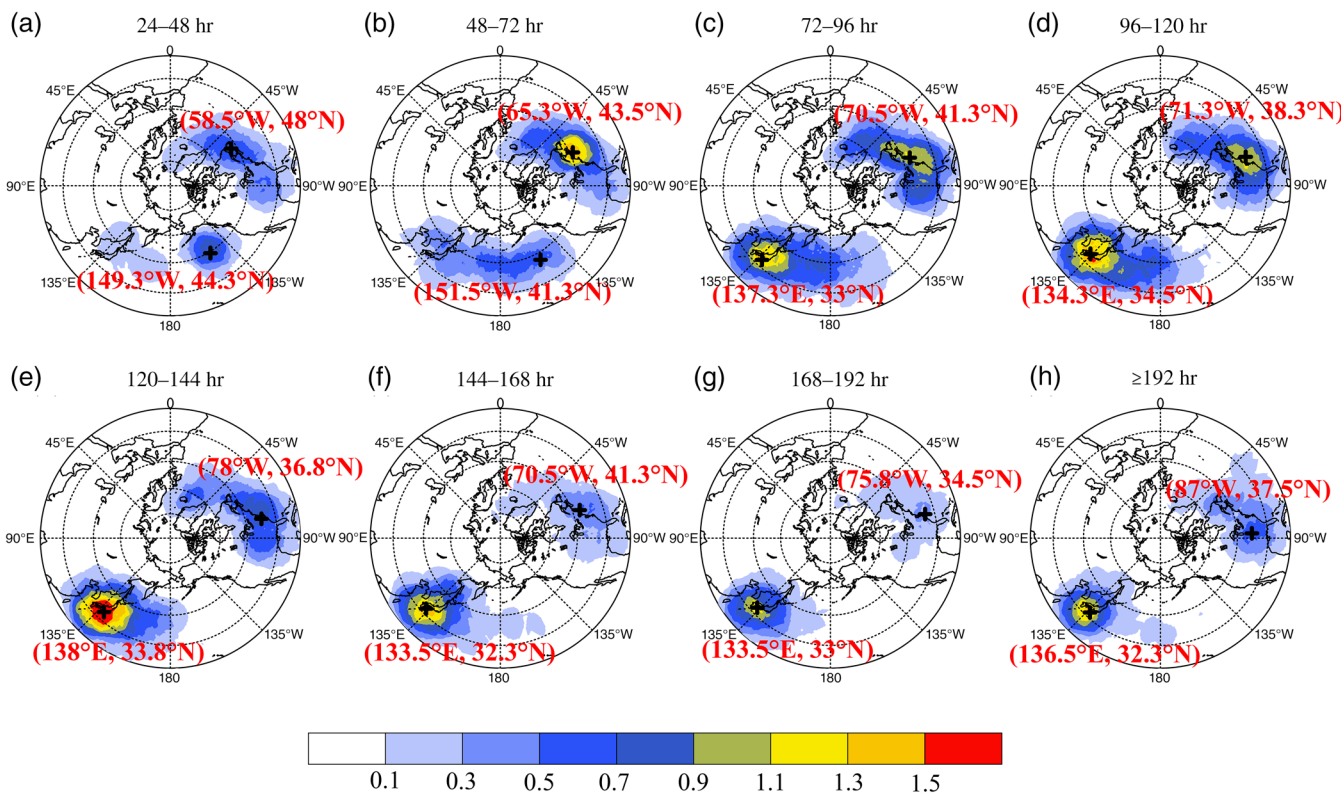


FIGURE 6 Distribution of the locations of formation of different types of ECs. (a) Distribution of ECs with lifespans of 24–48 hr (the black + marks the location where the maximum frequency appears). (b)–(h) As for (a), but for lifespans of 48–72 hr, 72–96 hr, 96–120 hr, 120–144 hr, 144–168 hr, 168–192 hr, and ≥ 192 hr, respectively [Colour figure can be viewed at wileyonlinelibrary.com]

TABLE 5 Occurrence frequency and percentage of different types of ECs relative to their maximum deepening rates

Maximum deepening rate (Bergeron)	All		PAT		AAT	
	Frequency	Percentage	Frequency	Percentage	Frequency	Percentage
1.0–1.1	574	27.6%	298	26.9%	270	28.1%
1.1–1.2	432	20.8%	230	20.8%	201	20.9%
1.2–1.3	324	15.6%	189	17.1%	133	13.8%
1.3–1.4	240	11.5%	122	11.0%	118	12.3%
1.4–1.5	162	7.8%	90	8.1%	72	7.5%
1.5–1.6	122	5.9%	63	5.7%	59	6.1%
1.6–1.7	85	4.1%	40	3.6%	45	4.7%
1.7–1.8	42	2.0%	26	2.3%	16	1.7%
1.8–1.9	42	2.0%	25	2.3%	17	1.8%
1.9–2.0	22	1.1%	12	1.1%	10	1.0%
2.0–2.1	14	0.7%	7	0.6%	7	0.7%
2.1–2.2	10	0.5%	3	0.3%	7	0.7%
2.2–2.3	4	0.2%	1	0.1%	3	0.3%
2.3–2.4	3	0.1%	1	0.1%	2	0.2%
≥ 2.4	2	0.1%	1	0.1%	1	0.1%
Total	2078	100.0%	1,108	100.0%	961	100.0%

Note: Values (in the fifth and seventh columns) in bold-italic, italic and bold mean that the differences between PAT and AAT pass the significance tests of levels 0.01, 0.05, and 0.1, respectively; whereas values in normal mean that the differences between PAT and AAT are not statistically significant.

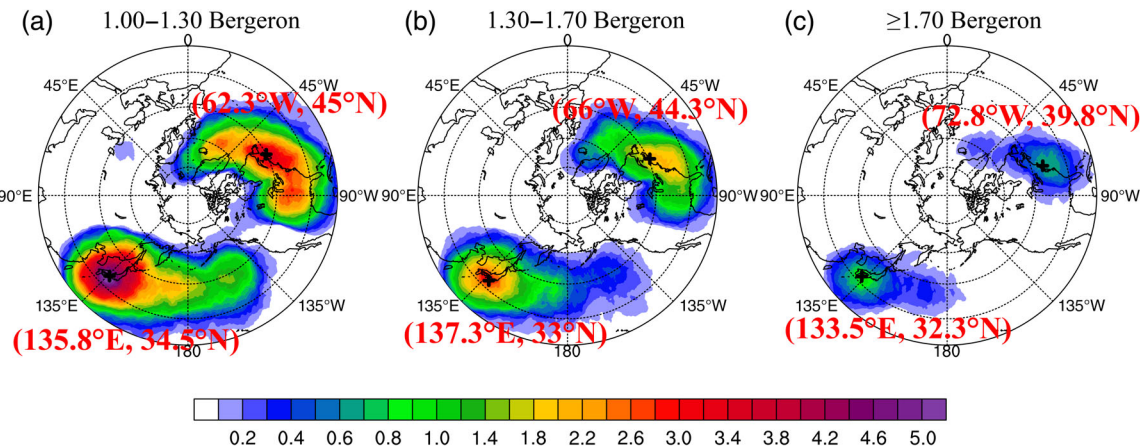


FIGURE 7 Locations of formation of (a) weak ECs (1–1.3 Bergeron), (b) moderate ECs (1.3–1.7 Bergeron), and (c) strong and super ECs (≥ 1.7 Bergeron). Shading represents the occurrence frequency. The red text refers to the position of maximum-occurrence-frequency [Colour figure can be viewed at wileyonlinelibrary.com]

ECs have two maximum-occurrence-frequency centres: one situated around the south of Japan and the other around the eastern coast of Canada (Figure 7b). For strong and super ECs, two maximum-occurrence-frequency centres are found to locate in the area of Kuroshio current and Gulf stream, similar to the situation of the moderate ECs (cf. Figure 7b,c).

A comparison of PAT with AAT ECs (Table 5) shows that the former have a larger number of ECs with a deepening rate of 1.0–1.6 Bergeron and 1.7–2.0 Bergeron (accumulated proportions are 95.3%/93.2% for PAT/AAT); a same number to the latter for the category of 2.0–2.1 Bergeron; whereas a less number for the categories of 1.6–1.7 Bergeron and ≥ 2.1 Bergeron. Overall, there are more PAT than AAT ECs in the groups with a deepening rate of 1.0–2.0 Bergeron (~1.2 times), whereas for the EC groups with a deepening rate more than 2.0 Bergeron, AAT ECs have an occurrence number that is ~1.5 times of that of PAT ECs. This is consistent with the comparison of the extremely long-lived ECs over the two oceans.

4 | FEATURES RELATED TO SURFACE WIND AND VERTICAL EXTENT

4.1 | Surface-wind-related features

In order to investigate the surface wind features, for each EC, the maximum surface wind speed and its position during the whole EC's lifecycle were investigated. From a comparison of the largest surface winds during each typical stage (Figure 8), it is found that, generally, the lowest wind speed occurs when an EC has just formed (i.e., at CFT) and the second lowest wind speed when it is about

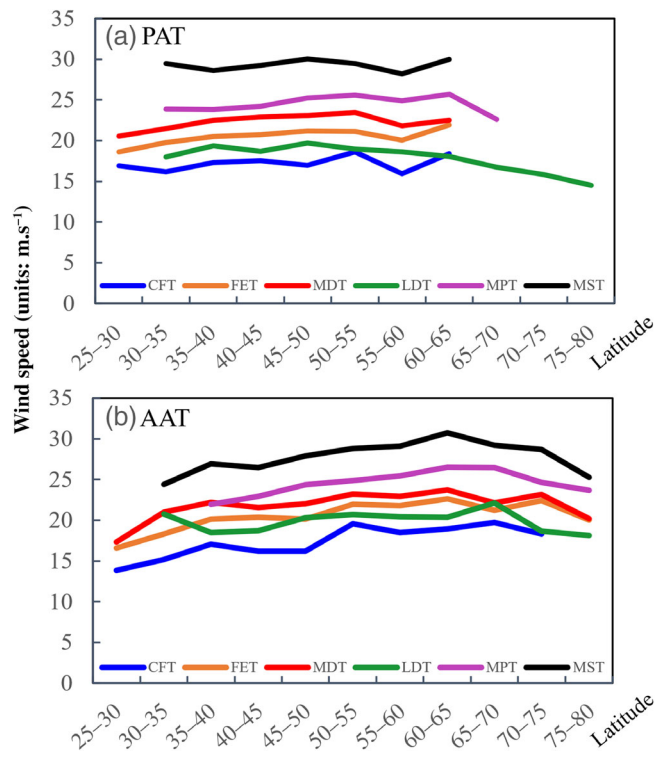


FIGURE 8 Zonal band (every 5° in latitude) averaged largest surface wind speeds (unit: m s^{-1}) associated with (a) PAT and (b) AAT ECs during each typical stage. Zonal bands where there are fewer than five ECs are not considered [Colour figure can be viewed at wileyonlinelibrary.com]

to dissipate (i.e., at LDT). From the time when an EC first reaches a deepening rate of 1 Bergeron (i.e., at FET) through the time when it has the highest deepening rate (i.e., at MDT) to the time when it reaches its lowest pressure (i.e., at MPT), the largest EC-associated surface wind becomes stronger. This corresponds well with the results

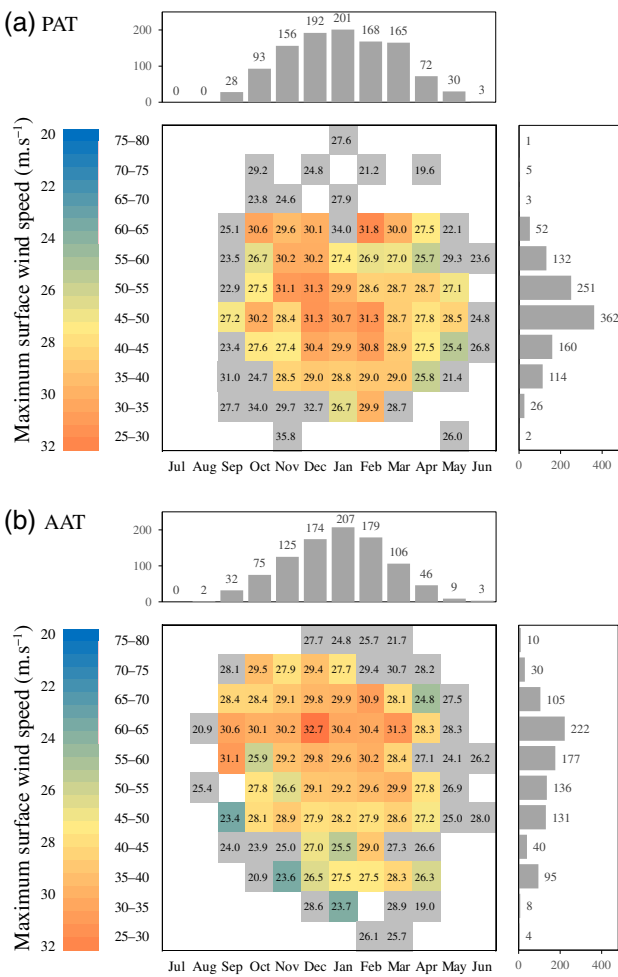


FIGURE 9 Monthly zonal band (every 5° in latitude) average maximum surface wind speeds (shaded blocks, unit: $\text{m}\cdot\text{s}^{-1}$) of (a) PAT and (b) AAT ECs, where grey blocks indicate that the values are calculated with fewer than five cyclones, the above histograms show the total numbers of maximum surface winds in the corresponding months, and the right histograms show the total numbers of maximum surface winds in specific zonal band [Colour figure can be viewed at wileyonlinelibrary.com]

documented by Simmonds (2000), who found that extratropical cyclones' size and intensity both increased, and their thickness became thicker as they entered their mature stage. As Table 3 shows, the maximum surface wind (during the whole EC lifespan) associated with an EC (i.e., at MST) tends to appear ~49 hr after EC formation. This stage is between the time when the EC reaches its maximum deepening rate and the time when it reaches its minimum pressure, which means that from MDT to MST, the largest EC-associated surface wind speed tends to increase, whereas from MST to MPT, it tends to decrease.

As the top histograms in Figure 9a and b show, for both PAT and AAT ECs, more than 50% of the maximum EC-associated surface wind appears in winter; spring and

autumn share similar proportions; and the lowest proportion is found in summer. This is consistent with their occurrence frequencies in each season (Table 2). Notable differences are found between the two types of ECs. For PAT ECs, the meridional distribution of occurrence of the maximum EC-associated surface wind has the form of a single-peak wave (right histogram in Figure 9a), with ~92% of the maximum wind occurring at $35^{\circ}\text{--}60^{\circ}\text{N}$. The highest proportion of ~32.7% appears at $45^{\circ}\text{--}50^{\circ}\text{N}$, with a mean wind speed of $\sim 30 \text{ m}\cdot\text{s}^{-1}$ (Figure 8a). For AAT ECs, the meridional distribution of occurrence of the maximum surface wind has the form of a double-peak wave during the period from December to March in the next year (right histogram in Figure 9b). One peak is at $60^{\circ}\text{--}65^{\circ}\text{N}$ (within the northern section of $45^{\circ}\text{--}70^{\circ}\text{N}$), which represents a proportion of ~23.1%, and the other is at $35^{\circ}\text{--}40^{\circ}\text{N}$, which accounts for ~9.8%. The mean maximum surface wind speed is $\sim 31 \text{ m}\cdot\text{s}^{-1}$ for the former peak (Figure 8a) and $\sim 27 \text{ m}\cdot\text{s}^{-1}$ for the latter (Figure 8b). As Figure 10 shows, the double peaks of AAT's maximum surface winds show consistent distributions to those of the BEC. The southern peak ($35^{\circ}\text{--}40^{\circ}\text{N}$) is separated from the northern section ($45^{\circ}\text{--}70^{\circ}\text{N}$) by a negative BEC (KE is converted into APE, which reduce wind speed) band within $40^{\circ}\text{--}45^{\circ}\text{N}$. This means that, the BEC which converts APE to KE is a key factor for the wind enhancement associated with ECs. Similar results have been found by Lim and Simmonds (2002), who also confirmed the key role of baroclinicity in ECs' development. Overall, for PAT ECs, the meridional variation of the zonal band-averaged maximum surface wind speed shows no obvious trend with increasing latitude (Figure 8a), whereas for AAT ECs, it mainly shows an increasing trend at $30^{\circ}\text{--}65^{\circ}\text{N}$ and a decreasing trend at $65^{\circ}\text{--}80^{\circ}\text{N}$ (Figure 8b). The meridional distribution of AAT-associated maximum surface wind speed is consistent with the meridional distribution of positive BEC (which means APE is converted into KE, which enhances wind) which also mainly increases at $30^{\circ}\text{--}65^{\circ}\text{N}$ and decreases at $65^{\circ}\text{--}80^{\circ}\text{N}$ (not shown). For PAT ECs, surface winds above $30 \text{ m}\cdot\text{s}^{-1}$ mainly appear from October to March in the next year, within the zonal band $40^{\circ}\text{--}65^{\circ}\text{N}$ (Figure 9a). The maximum mean wind speed of $31.8 \text{ m}\cdot\text{s}^{-1}$ occurs within $60^{\circ}\text{--}65^{\circ}\text{N}$, in February; however, it should be noted that some PAT ECs at lower latitudes ($25^{\circ}\text{--}35^{\circ}\text{N}$) can reach maximum surface wind speeds of $34 \text{ m}\cdot\text{s}^{-1}$ or more. For AAT ECs, surface winds above $30 \text{ m}\cdot\text{s}^{-1}$ mainly appear from September to March in the next year (a wider timespan than that of PAT ECs) (Figure 9b), within the zonal band $55^{\circ}\text{--}70^{\circ}\text{N}$ (much narrower than that of PAT ECs). Of these, 70% occur in the zonal band $60^{\circ}\text{--}65^{\circ}\text{N}$, and the maximum mean wind speed of $32.7 \text{ m}\cdot\text{s}^{-1}$ also appears in this band. Unlike PAT ECs, at lower latitudes ($25^{\circ}\text{--}35^{\circ}\text{N}$), the maximum surface wind

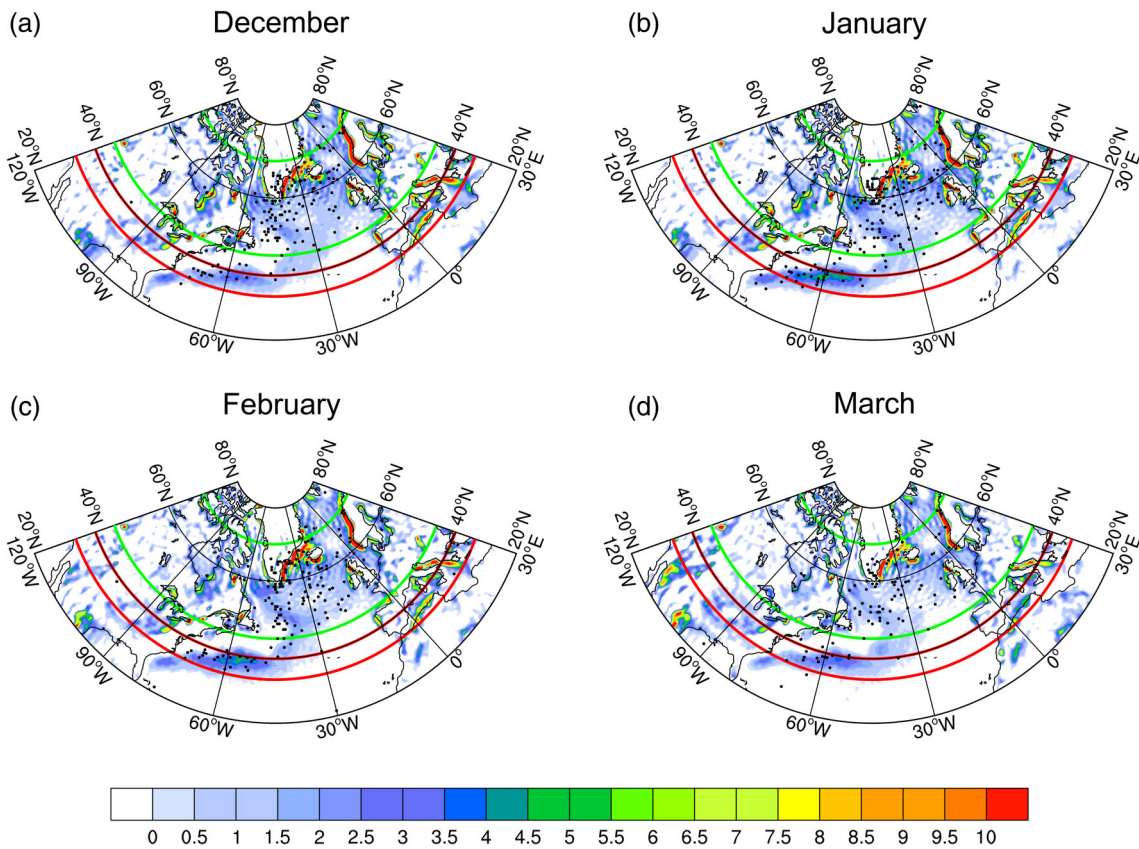


FIGURE 10 Monthly mean 900-hPa BEC (shading, unit: $\text{W}\cdot\text{kg}^{-1}$), where the green arcs outline the northern section of $45^{\circ}\text{--}70^{\circ}\text{N}$ (shown in the right histogram of figure 9b), the red arcs outline the southern peak of $35^{\circ}\text{--}40^{\circ}\text{N}$, and the black dots mark the locations of EC-associated maximum surface winds [Colour figure can be viewed at wileyonlinelibrary.com]

speed is generally below $29 \text{ m}\cdot\text{s}^{-1}$, this shows that at lower latitudes, the maximum surface wind speed of PAT ECs is higher than that for AAT ECs.

For PAT ECs, their quadrant I (northeastern section) accounts for the largest proportion of maximum surface wind during the whole EC's lifecycle (~45.8%) (Figure 11a), and the mean wind speed within this quadrant is also strongest (~ $30.5 \text{ m}\cdot\text{s}^{-1}$). More than 75% of these maximum surface winds appear within 700 km of the EC centres (Figure 11c). Quadrants IV (southeastern section), II (northwestern section), and III (southwestern section) share similar proportions (with maximum difference < 2%) and their mean wind speeds are also similar (with maximum difference < $1 \text{ m}\cdot\text{s}^{-1}$) (Figure 11a). In quadrants II and III, most (>75%) maximum surface winds occur within 600 km of the ECs' centres (Figure 11c), whereas the corresponding distance for quadrant IV is 1,000 km. Overall, the PAT ECs in the eastern section (quadrants I and IV) have larger proportions (~2 times) and stronger wind speeds than those in the western section (quadrants II and III). For AAT ECs, quadrant I also has the largest proportion of maximum surface wind (~34.3%) (Figure 11b) and the strongest

mean wind speed (~ $30.4 \text{ m}\cdot\text{s}^{-1}$). Similar to the situation with PAT ECs, most of the maximum surface winds occur within 700 km of the ECs' centres (Figure 11c). Quadrant III ranks in second place in terms of proportion (~25.0%), whereas quadrants II and IV share similar proportions. Compared with PAT ECs, in quadrant III, AAT ECs have similar distances that are between the locations of the maximum surface wind and the EC centre (Figure 11c), whereas in quadrants II and IV, the maximum surface winds tend to appear ~100 km farther and ~100 km closer to the ECs' centres, respectively. In terms of mean maximum surface wind speed, quadrant II is the second strongest (~ $29.3 \text{ m}\cdot\text{s}^{-1}$) (Figure 11b), whereas quadrants III and IV have similar wind speeds of ~ $27 \text{ m}\cdot\text{s}^{-1}$.

The northeastern quadrant of both PAT and AAT has the largest proportion and strongest intensity of maximum surface winds (Figure 11a,b). As Figure 12 shows, the strongest positive BEC appears within quadrant I for both types of ECs. This means that the conversion from APE to KE is most intense within quadrant I, which is consistent with the distribution features of maximum surface wind (Figure 11a,b). Our findings are consistent

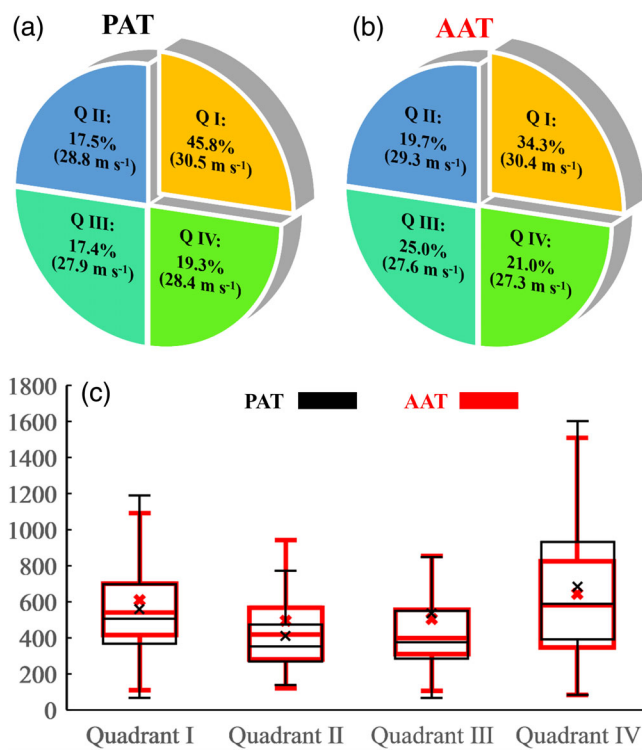


FIGURE 11 Proportions of occurrence of maximum surface winds in quadrants I–IV (Q I–Q IV), and the corresponding quadrant-averaged maximum surface winds ($m\cdot s^{-1}$) for (a) PAT and (b) AAT ECs. (c) Boxplot of the distance between the location of the maximum surface wind and the centre of the EC (unit: km), where the red and black plots are for AAT and PAT ECs, respectively, the solid lines within boxes show the median values, and the crosses show the average values. The extent of the boxes corresponding to 25% (first quartile), 75% (third quartile), and whiskers corresponds to (third quartile) – 1.5 * (interquartile range) and (first quartile) + 1.5 * (interquartile range). The outliers are removed [Colour figure can be viewed at wileyonlinelibrary.com]

with the EC cases documented in Hart *et al.* (2017) and Baker (2009), whereas it is different from the EC case reported by Browning *et al.* (1998), associated with which the maximum surface wind appeared in quadrant IV. Overall, the western section of AAT ECs has a smaller proportion of maximum surface winds than that of the eastern section (Figure 11b), and a comparable wind speed. Compared with PAT ECs, a larger proportion of maximum surface winds appear in AAT ECs' western section, with their mean wind speeds comparable to those of the western section of PAT ECs (cf. Figure 11a,b). From Figure 12 it is clear that, compared to that of PAT ECs, the western section of AAT ECs has a larger positive BEC and a smaller (i.e., absolute value) negative BEC. This means that compared to that of PAT ECs, more energy is converted from APE to KE for AAT ECs within their western sections. This is a possible reason for the larger

proportion of maximum surface winds that appear in AAT ECs' western section.

4.2 | Vertical-extent-related features

From cyclone formation (i.e., at CFT) to the time when an EC reaches its minimum central pressure (i.e., at MPT), its top level mainly extends upward with time (Figures 13a–d and 14), and, after reaching its highest top level (i.e., at HTT), its vertical extent shrinks with time (Figures 13d,e and 14). This is consistent with the evolutionary features of extratropical cyclones' vertical extents documented in Fu *et al.* (2015) and Li *et al.* (2019). Most ECs have their smallest vertical extent just after formation, although a small proportion of PAT ECs (at 60° – 80° N) are found to reach their lowest top levels just before dissipation (Figure 14). At CFT, FET, and MDT, the vertical extents of both PAT and AAT ECs generally become thicker with increasing latitude ($p < 0.05$) (Figures 13a–c and 14).

On average, PAT ECs tend to reach their highest top levels \sim 2 hr after they reach their minimum central pressure (i.e., at MPT) (Table 3), whereas the corresponding time for AAT ECs is \sim 3 hr before their MPT. This means that the highest top level of an EC usually appears around the MPT. More than 60% of ECs have a highest top level above 300 hPa (Table 6), which means that most ECs are deep cyclones. This is consistent with the findings in Fu *et al.* (2018) and Pepler and Dowdy (2020). By contrast, it is rare for an EC (<3.5%) to extend only to the lower troposphere (below 700 hPa). The proportion of ECs that have their highest top levels around 500 hPa (600–400 hPa) is \sim 12% (Table 6). Over 85% of PAT ECs reach their highest top level in the zonal band of 40° – 60° N (right histogram in Figure 15a), with the largest proportion (30.9%) appearing at 50° – 55° N. Over 73% of AAT ECs reach their highest top level (also reach the maximum vertical extent) in the zonal band 45° – 65° N, with the largest proportion (23.5%) appearing at 60° – 65° N (right histogram in Figure 15b). Overall, PAT ECs tend to reach their highest top levels within regions at lower latitudes than those of AAT ECs (cf. the shaded blocks in Figure 15a,b), and their maximum vertical extents are greater than those of AAT ECs (cf. the black solid lines in Figure 14a,b). As Figure 16 shows, ascending motions are stronger for PAT than those of AAT, which provides more favourable conditions for their upward extending. This is an important reason for why PAT's top level is generally higher than that of AAT. In terms of seasonal distribution, more than half of ECs reach their highest

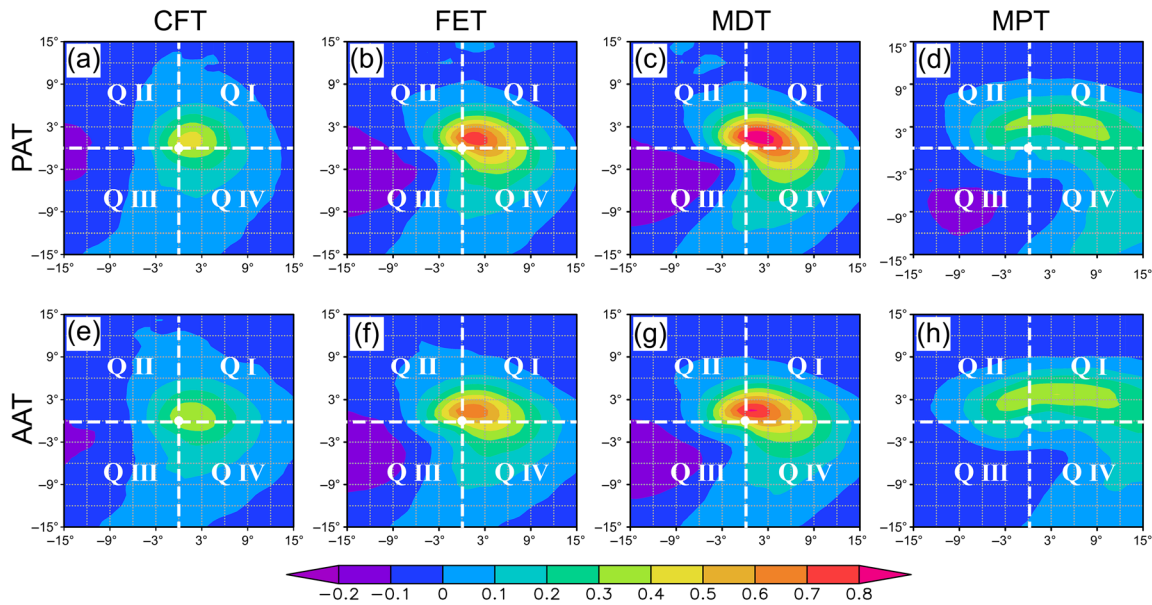


FIGURE 12 Composite (based on the Lagrange viewpoint) vertical averaged (from surface to 500 hPa) baroclinic energy conversion (shading, unit: $\text{W} \cdot \text{kg}^{-1}$) of PATs and AATs at typical stages, where the big white dot shows ECs' centres, and the white dash lines mark the four quadrants: Q I, Q II, Q III, and Q IV [Colour figure can be viewed at [wileyonlinelibrary.com](#)]

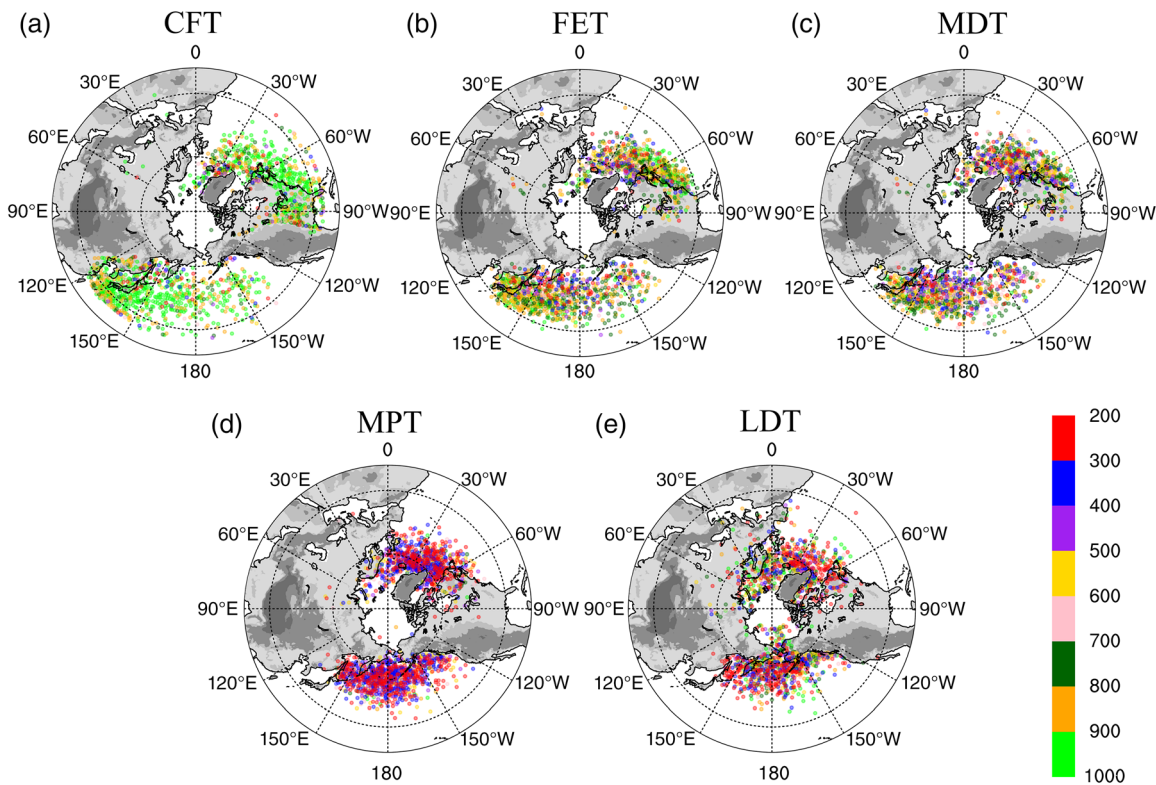


FIGURE 13 Spatial distribution of top levels of ECs at different stages: (a) CFT; (b) FET; (c) MDT; (d) MPT; (e) LDT. The points indicate the surface centres of the ECs, and the colours of the points indicate their top levels (unit: hPa) [Colour figure can be viewed at [wileyonlinelibrary.com](#)]

top levels in winter (top histograms in Figure 15a,b), the proportion in spring and autumn are similar to each other, and the lowest proportion appears in summer.

This is consistent with the seasonal occurrence frequency of ECs (Table 2). On average, for both types of ECs, top levels higher than 250 hPa mainly appear in September,

October, April, and May (Figure 15), whereas in other months, the highest top levels mainly range from 400 to 250 hPa. This is consistent with the fact that EC-associated ascending motions are stronger in September, October, April, and May (not shown).

The mean highest top levels of PAT and AAT ECs generally become higher as their minimum central pressure decreases (Figure 17a,b). Around 73% of PAT ECs have a minimum central pressure in the range 965–985 hPa, and their mean highest top levels are between

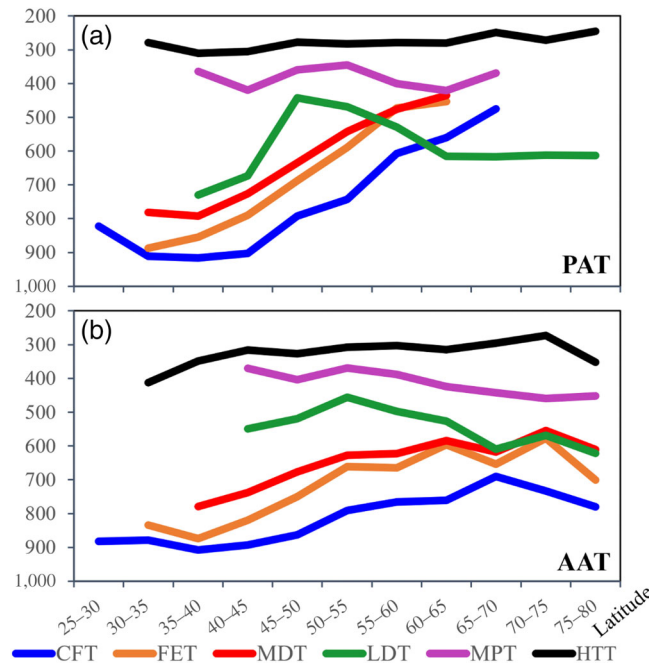


FIGURE 14 Zonal band (every 5° in latitude) average top levels (unit: hPa) of (a) PAT and (b) AAT ECs during each typical stage. Zonal bands where there are fewer than five ECs are not considered [Colour figure can be viewed at wileyonlinelibrary.com]

TABLE 6 Frequency and percentage of different vertical extents of ECs

Top level (hPa)	All		PAT		AAT	
	Frequency	Percentage	Frequency	Percentage	Frequency	Percentage
1,000–900	5	0.2%	2	0.2%	3	0.3%
900–800	17	0.8%	2	0.2%	15	1.6%
800–700	19	0.9%	7	0.6%	12	1.2%
700–600	81	3.9%	26	2.3%	54	5.6%
600–500	119	5.7%	60	5.4%	59	6.1%
500–400	129	6.2%	63	5.7%	65	6.8%
400–300	389	18.7%	214	19.3%	175	18.2%
300–200	1,319	63.5%	734	66.2%	578	60.1%
Total	2078	100.0%	1,108	100.0%	961	100.0%

Note: Values (in the fifth and seventh columns) in bold-italic, italic and bold mean that the differences between PAT and AAT pass the significance tests of levels 0.01, 0.05, and 0.1, respectively; whereas values in normal mean that the differences between PAT and AAT are not statistically significant.

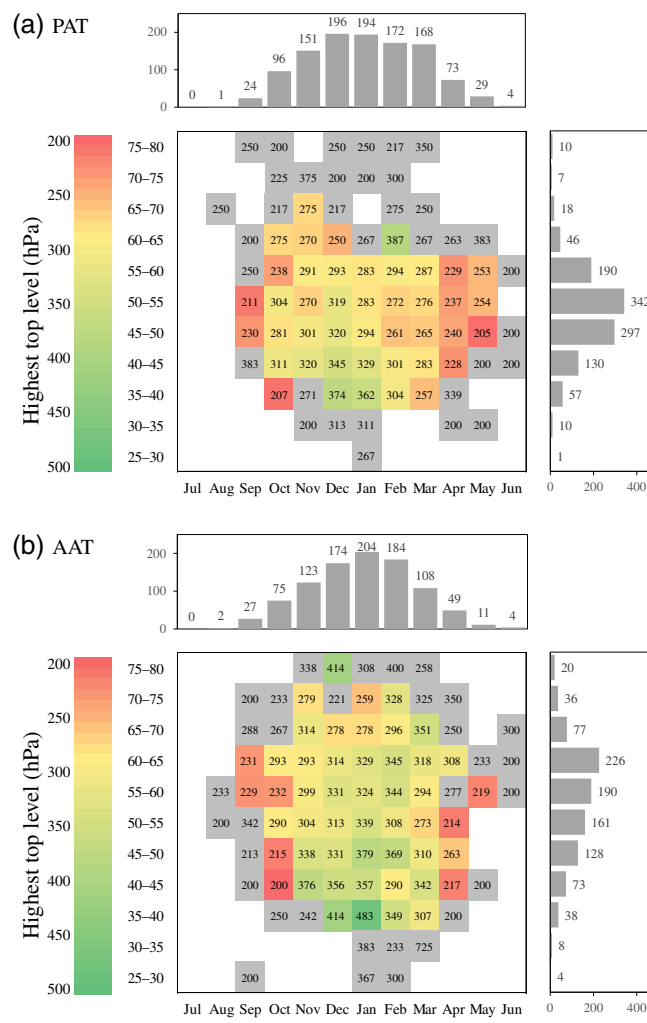


FIGURE 15 Monthly zonal band (every 5° in latitude) averaged highest top levels (shaded blocks, unit: hPa) of (a) PAT and (b) AAT ECs. Grey blocks indicate that the values are calculated with fewer than five cyclones, and the histograms show the total numbers of highest top levels in the corresponding months (above) and specific zonal band (right) [Colour figure can be viewed at wileyonlinelibrary.com]

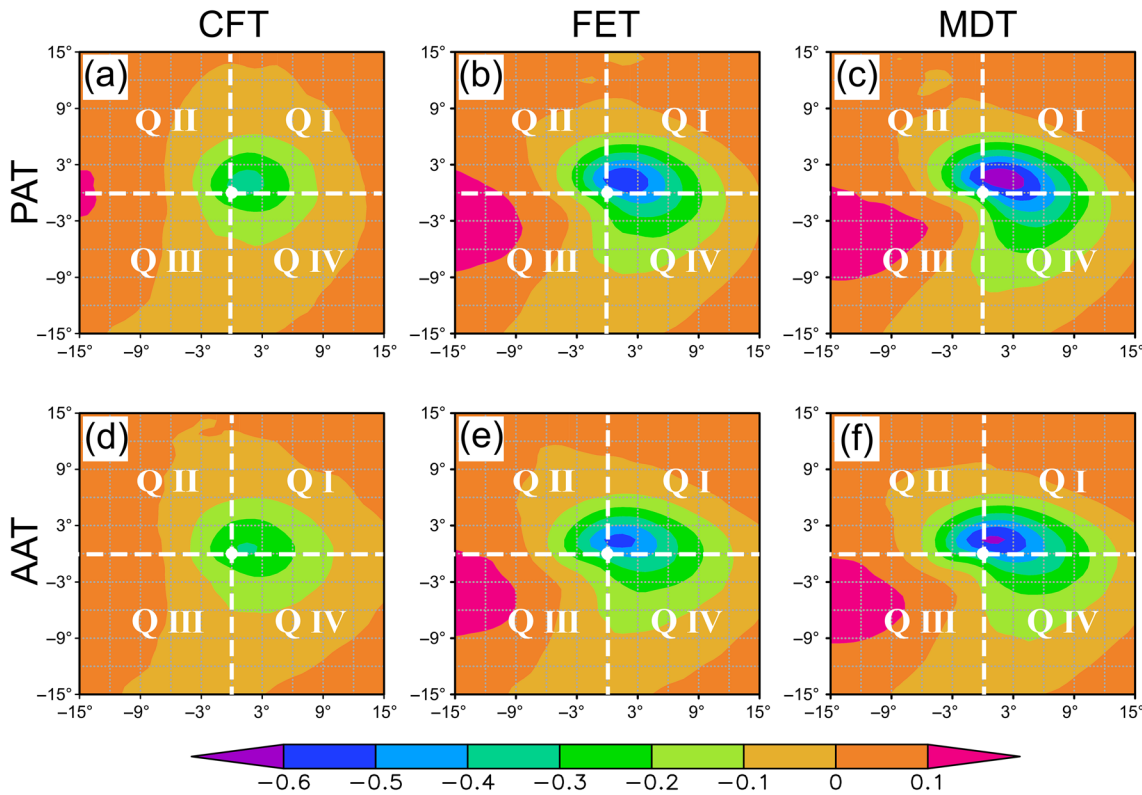


FIGURE 16 Composite (based on the Lagrange viewpoint) vertical averaged (from surface to 200 hPa) vertical velocity (shading, unit: $\text{Pa} \cdot \text{s}^{-1}$) of PAT and AAT at typical stages, where the big white dot shows ECs' centres, and the white dash lines mark the four quadrants: Q I, Q II, Q III, and Q IV [Colour figure can be viewed at wileyonlinelibrary.com]

325 and 250 hPa (Figure 17a). For AAT ECs, ~74.6% of their minimum central pressure is in the range 965–985 hPa, and the mean highest top levels of these ECs are between 350 and 250 hPa (Figure 17b). As Figure 17c,d shows, the mean highest top levels of PAT and AAT ECs show an overall upward extending trend as their deepening rate increases. The highest top levels of weak PAT and AAT ECs are between 300 and 275 hPa and between 325 and 300 hPa, respectively. These levels are both lower than those of strong and super ECs (between 275 and 225 hPa for PAT, and between 325 and 225 hPa for AAT). The mean highest top levels of PAT ECs show no obvious trends of variation with their maximum surface winds (Figure 17e). This is also true for those AAT ECs that have maximum surface wind speeds above $32 \text{ m} \cdot \text{s}^{-1}$ (Figure 17f). However, for those AAT ECs that have maximum surface wind speeds below $32 \text{ m} \cdot \text{s}^{-1}$, the mean highest top levels show an obvious upward extending trend as their maximum surface wind speed increases.

Due to strong vertical wind shear, the vertical extents of ECs show notable vertical tilting. Two factors are defined to describe the tilting, the first is the distance between an EC's top-level centre and its surface centre (DTS), which indicates the tilting

magnitude; the second is the azimuth of an EC's top-level centre relative to its surface centre (ATS), which denotes the tilting direction. Overall, for DTS, PAT and AAT showed similar features (Figure 18a). The fastest increase and decrease of DTS appear in the periods of CFT-FET (i.e., from CFT to FET) and MDT-MPT, respectively. The former corresponds to the rapid enhancement in baroclinity, whereas, the latter is consistent with the quick weakening of baroclinity. The periods of FET-MDT and MPT-LDT feature slow variations of DTS, respectively, implying that baroclinity during these periods change slowly. The largest DTSs tend to appear at MDT (Figure 18a), when ECs' vertical extent grow rapidly. After the ECs reach their highest top-levels (i.e., MPT; Table 3), their DTSs decrease notably, as baroclinity associated with them weaken. The BEC from APE (APE is an effective indicator for baroclinity) to KE is an important reason for ECs' development and reduction in baroclinity.

For ATS, PAT and AAT show similar features (Figure 18b). Around CFT, when the ECs are weak and develop slowly, they show tilting in all directions. From FET to MDT, as the ECs develop rapidly, their ATS keeps concentrated, which is mainly located within 225° – 355° . This indicates that the ECs mainly

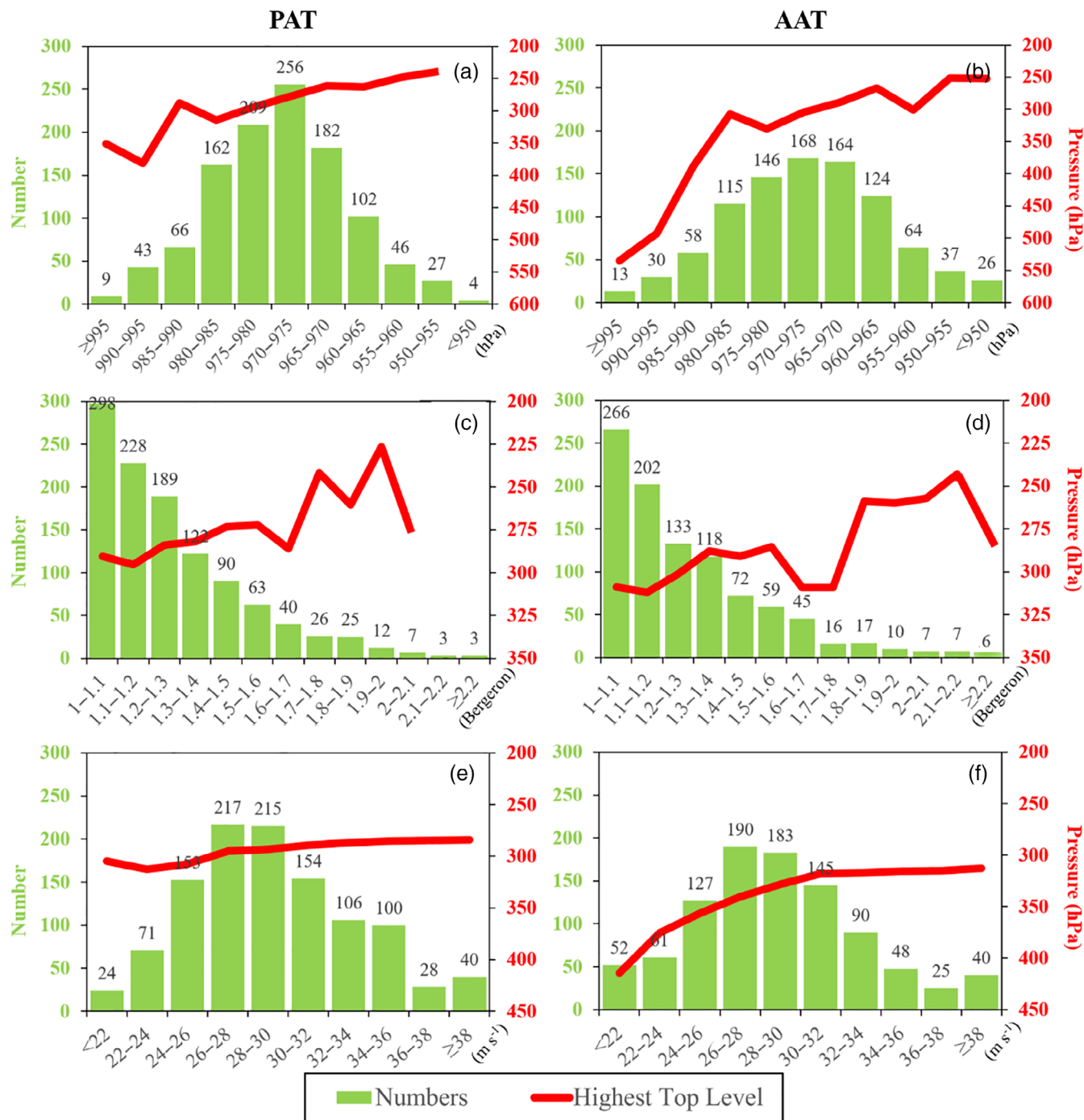
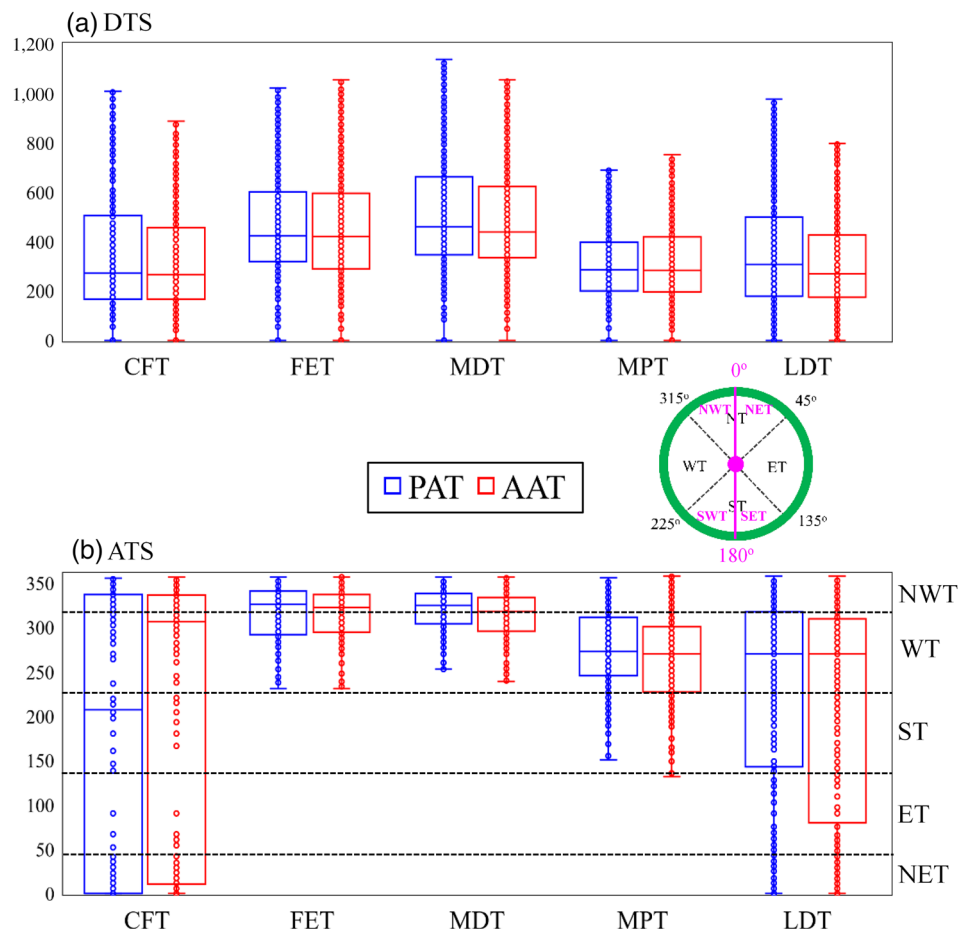


FIGURE 17 Highest top levels of (a) PAT and (b) AAT ECs (unit: hPa) relative to their respective minimum pressures (unit: hPa). Highest top levels of (c) PAT and (d) AAT ECs (unit: hPa) relative to their respective maximum deepening rates (unit: Bergeron). Highest top levels of (e) PAT and (f) AAT ECs (unit: hPa) relative to their respective maximum surface wind speeds (unit: m·s⁻¹) [Colour figure can be viewed at wileyonlinelibrary.com]

tilt to the west or northwest with height. After the ECs reach their highest top-levels (around MPT), over a half of them show westward tilting, and a small proportion of them begin to tilt southward. As ECs enter the LDT, eastward and northeast tilting appear again,

but less than that of CFT. Overall, ATS does not show a consistent variation feature with that of DTS or ECs' vertical extent (Figure 18). The value range of ATS (larger value range means more tilting directions) is large at CFT and LDT (Figure 18b), when the

FIGURE 18 Panel (a) is the boxplot of the distance between ECs' top centres and their surface centres (DTS; unit: km). Panel (b) is the boxplot of the azimuth of an EC's top-level centre relative to its surface centre (ATS; units degree). NT = northward tilting (from bottom up), NWT = northwestward tilting, NET = northeastward tilting, WT = westward tilting, SWT = southwestward tilting, SET = southeastward tilting, ST = southward tilting, and ET = eastward tilting, which are shown by the green circle with purple centre (denotes the cyclone's surface centre). The solid line within a box marks the median value, the open circles show the values within the whiskers, the extent of the boxes corresponding to 25% (first quartile), 75% (third quartile), and whiskers corresponds to (third quartile) – 1.5 * (interquartile range) and (first quartile) + 1.5 * (interquartile range) [Colour figure can be viewed at wileyonlinelibrary.com]



deepening rate is small; whereas, at FET and MDT, when the deepening rate is large, the value range is small.

5 | CONCLUSION AND DISCUSSION

In this study, based on 6-hourly $0.75^\circ \times 0.75^\circ$ ERA-I reanalysis data from 1979 to 2018, a statistical analysis has been conducted on ECs in the Northern Hemisphere. The ESSD method has been used to identify ECs during the 40-year period. After manual verification, a total of 2078 ECs have been determined, which means that ~52 ECs appear in the Northern Hemisphere every year. This figure is obviously more than that found by Black and Pezza (2013) (~18 ECs per year) and Allen *et al.* (2010) (~36 ECs per year), but is about a half of the result found by Fu *et al.* (2020) (~103 ECs per year) (All of these three results are based on the ERA-Interim dataset). This is comparable to the 46 diagnosed by Lim and Simmonds (2002) which are based on the NCEP-DOE II dataset. Differences in EC definitions and detection methods are the main reasons for these differences. The Northern Pacific and

Northern Atlantic Oceans are found to be the two most important source regions for ECs in the Northern Hemisphere. The mean deepening rates of PAT and AAT are 1.27 and 1.28 Bergeron, respectively, which are ~15% smaller than those found by Fu *et al.* (2020). ECs tend to move northeastward after formation, and winter is the most active season for their formation. This is consistent with the results found by most previous EC statistical studies (Yoshida and Asuma, 2004; Sanders and Gyakum, 1980; Allen *et al.*, 2010; Fu *et al.*, 2020). Their occurrence frequency tends to (a) decrease as their deepening rate grows larger (similar to those found by Fu *et al.* (2020)), with ~64% of them being weak ECs (≤ 1.3 Bergeron), and (b) first increase as their lifespans lengthen, and then decrease, with ~76% of them lasting for 48–168 hr. Overall, PAT ECs have a larger occurrence number and a longer mean lifespan ($p < 0.01$). These are similar to the findings of previous studies (e.g., Yoshida and Asuma, 2004; Allen *et al.*, 2010; Zhang *et al.*, 2017; Fu *et al.*, 2020). Furthermore, we find that (a) the average location of formation of ECs undergoes an obvious westward and equatorward shift from September to April in the next year, (b) overall, PAT ECs tend to form in regions at lower latitudes than AAT ECs, (c) among the extreme ECs that have a deepening rate

more than 2.0 Bergeron or with a longer lifespan more than 10 days, AAT ECs tend to have a larger occurrence number than PAT ECs.

There have been a number of new findings about the surface winds and vertical extent of ECs: (a) The maximum surface wind associated with an EC tends to appear between the time when the EC reaches its maximum deepening rate and the time when it reaches its minimum central pressure. (b) For PAT ECs, ~32.7% of their associated maximum surface wind occurs at 45°–50°N, with a mean speed of $\sim 30 \text{ m}\cdot\text{s}^{-1}$; for AAT ECs, ~23.1% of their maximum surface wind occurs at 60°–65°N, with a mean speed of $\sim 31 \text{ m}\cdot\text{s}^{-1}$. (c) More damaging winds tend to occur in the eastern section of ECs, of which the northeastern quadrant has the largest proportion of maximum surface winds and strongest wind speeds (mainly within 700 km from the EC centres). (d) Over 60% of ECs belong to a type of vertically deep cyclone (with top levels above 300 hPa), and they tend to reach their highest top level around the time when they gain their minimum central pressure. (e) PAT ECs tend to reach their highest top levels within regions at lower latitudes than those of AAT ECs, and their maximum vertical extents are greater than those of AAT ECs. (f) The highest top levels of ECs exhibit an overall upward extending trend as their minimum central pressure decreases or their deepening rate increases, whereas for the maximum EC-associated surface wind, an upward extending trend with increasing maximum surface wind is obvious for AAT ECs only when the wind speed is below $32 \text{ m}\cdot\text{s}^{-1}$.

ACKNOWLEDGMENTS

The authors thank ECMWF (European Centre for Medium-Range Weather Forecasts) for providing the data used in this study (<https://www.ecmwf.int/en/forecasts/datasets/reanalysis-datasets/era-interim/>). This research was supported by the National Key R&D Program of China (Grant No. 2018YFC0809400), the National Natural Science Foundation of China (Grant Nos. 41775046 and 42075002), and the Youth Innovation Promotion Association, Chinese Academy of Sciences, and the National Key Scientific and Technological Infrastructure project “Earth System Science Numerical Simulator Facility”.

AUTHOR CONTRIBUTIONS

Lizhi Jiang: Data curation; formal analysis; investigation; methodology; software; validation; visualization; writing - original draft; writing-review & editing.
Shenming Fu: Conceptualization; funding acquisition; methodology; project administration; resources; software; supervision; visualization; writing - original draft; writing-review & editing. **Jianhua Sun:** Funding acquisition; project administration; supervision. **Rui Fu:**

Resources; software. **Wanli Li:** Data curation; resources. **S Zhao:** Supervision. **Hui Wang:** Resources.

ORCID

Li-Zhi Jiang  <https://orcid.org/0000-0003-1273-9788>
Shen-Ming Fu  <https://orcid.org/0000-0001-9670-0607>

REFERENCES

- Allen, J.T., Pezza, A.B. and Black, M.T. (2010) Explosive cyclogenesis: a global climatology comparing multiple Reanalyses. *Journal of Climate*, 23, 6468–6484.
- Baker, L. (2009) Sting jets in severe northern European wind storms. *Weather*, 64, 143–148.
- Binder, H., Boettcher, M., Joos, H. and Wernli, H. (2016) The role of warm conveyor belts for the intensification of extratropical cyclones in northern hemisphere winter. *Journal of the Atmospheric Sciences*, 73, 3997–4020.
- Black, M.T. and Pezza, A.B. (2013) A universal, broad-environment energy conversion signature of explosive cyclones. *Geophysical Research Letters*, 40, 452–457.
- Bosart, L.F. (1981) The Presidents' day snowstorm of 18–19 February 1979: a subsynoptic-scale event. *Monthly Weather Review*, 109, 1542–1566.
- Brâncuș, M., Schultz, D.M., Antonescu, B., Dearden, C. and Ștefan, S. (2019) Origin of strong winds in an explosive Mediterranean extratropical cyclone. *Monthly Weather Review*, 147, 3649–3671.
- Browning, K.A. (2004) The sting at the end of the tail: damaging winds associated with extratropical cyclones. *Quarterly Journal of the Royal Meteorological Society*, 130, 375–399.
- Browning, K.A., Vaughan, G. and Panagi, P. (1998) Analysis of an ex-tropical cyclone after its re-intensification as a warm-core extratropical cyclone. *Quarterly Journal of the Royal Meteorological Society*, 124, 2329–2356.
- Campa, J. and Wernli, H. (2012) A PV perspective on the vertical structure of mature Midlatitude cyclones in the northern hemisphere. *Journal of the Atmospheric Sciences*, 69, 725–740.
- Campins, J., Genovés, A., Picornell, M.A. and Jansà, A. (2011) Climatology of Mediterranean cyclones using the ERA-40 dataset. *International Journal of Climatology*, 31, 1596–1614.
- Catto, J.L., Madonna, E., Joos, H., Rudeva, I. and Simmonds, I. (2015) Global relationship between fronts and warm conveyor belts and the impact on extreme precipitation. *Journal of Climate*, 28, 8411–8429.
- Chen, S.J., Kuo, Y.H., Zhang, P.Z. and Bai, Q.F. (1992) Climatology of explosive cyclones off the east-Asian coast. *Monthly Weather Review*, 120, 3029–3035.
- Colle, B.A., Zhang, Z., Lombardo, K.A., Chang, E., Liu, P. and Zhang, M. (2013) Historical evaluation and future prediction of eastern north American and Western Atlantic extratropical cyclones in the CMIP5 models during the cool season. *Journal of Climate*, 26, 6882–6903.
- Davis, C.A., Grell, E.D. and Shapiro, M.A. (1996) The balanced dynamical nature of a rapidly intensifying oceanic cyclone. *Monthly Weather Review*, 124, 3–26.
- Devore, J. (2004) *Probability and Statistics: For Engineering and the Sciences*, 5th edition. Beijing: Higher Education Press.
- Ding, Z., Wang, J. and He, J. (1998) Statistical study of explosive cyclones. *Journal of Nanjing Institute of Meteorology (in Chinese)*, 21, 424–431.

- European Centre for Medium-Range Weather Forecasts (2009). ERA-Interim Project, <https://doi.org/10.5065/D6CR5RD9>, Research Data Archive at the National Center for Atmospheric Research, Computational and Information Systems Laboratory, Boulder, CO.
- Flocas, H.A., Simmonds, I., Kouroutzoglou, J., Keay, K., Hatzaki, M., Bricolais, V. and Asimakopoulos, D. (2010) On cyclonic tracks over the eastern Mediterranean. *Journal of Climate*, 23, 5243–5257.
- Fu, G., Sun, Y., Sun, J. and Li, P. (2020) A 38-year climatology of explosive cyclones over the northern hemisphere. *Advances in Atmospheric Sciences*, 37, 143–159.
- Fu, S. and Sun, J. (2012) Circulation and Eddy kinetic energy budget analyses on the evolution of a Northeast China cold vortex (NCCV) in May 2010. *Journal of the Meteorological Society of Japan*, 90, 553–573.
- Fu, S., Sun, J. and Sun, J. (2014) Accelerating two-stage explosive development of an extratropical cyclone over the northwestern Pacific Ocean: a piecewise potential vorticity diagnosis. *Tellus A: Dynamic Meteorology and Oceanography*, 66(1), 23210.
- Fu, S., Li, W., Sun, J., Zhang, J. and Zhang, Y. (2015) Universal evolution mechanisms and energy conversion characteristics of long-lived mesoscale vortices over the Sichuan Basin. *Atmospheric Science Letters*, 16, 127–134.
- Fu, S.M., Zhang, J.P., Sun, J.H. and Zhao, T.B. (2016) Composite analysis of long-lived mesoscale vortices over the middle reaches of the Yangtze River valley: octant features and evolution mechanisms. *Journal of Climate*, 29, 761–781.
- Fu, S., Sun, J., Li, W. and Zhang, Y. (2018) Investigating the mechanisms associated with the evolutions of twin extratropical cyclones over the Northwest Pacific Ocean in mid-January 2011. *Journal of Geophysical Research*, 123, 4088–4109.
- Grigoriev, S., Gulev, S. and Zolina, O. (2000) Innovative software facilitates cyclone tracking and analysis. *Eos, Transactions American Geophysical Union*, 81, 170–170.
- Hart, N.C.G., Gray, S.L. and Clark, P. (2017) Sting-jet windstorms over the North Atlantic: climatology and contribution to extreme wind risk. *Journal of Climate*, 30, 5455–5471.
- Hewson, T. and Neu, U. (2015) Cyclones, windstorms and the IMILAST project. *Tellus A*, 67, 27128.
- Hirata, H., Kawamura, R., Kato, M. and Shinoda, T. (2015) Influential role of moisture supply from the Kuroshio/Kuroshio extension in the rapid development of an extratropical cyclone. *Monthly Weather Review*, 143, 4126–4144.
- Iwao, K., Inatsu, M. and Kimoto, M. (2012) Recent changes in explosively developing extratropical cyclones over the winter northwestern Pacific. *Journal of Climate*, 25, 7282–7296.
- Jia, Y. and Zhao, S. (1994) A diagnostic study of explosive development of extratropical cyclone over East Asia and West Pacific Ocean. *Advances in Atmospheric Sciences*, 11, 251–270.
- Jiang, L., Fu, S. and Sun, J. (2020) New method for detecting extratropical cyclones: the eight-section slope detecting method. *Atmospheric and Oceanic Science Letters*, 13, 436–442.
- Kouroutzoglou, J., Flocas, H.A., Keay, K., Simmonds, I. and Hatzaki, M. (2011a) Climatological aspects of explosive cyclones in the Mediterranean. *International Journal of Climatology*, 31, 1785–1802.
- Kouroutzoglou, J., Flocas, H.A., Simmonds, I., Keay, K. and Hatzaki, M. (2011b) Assessing characteristics of Mediterranean explosive cyclones for different data resolution. *Theoretical and Applied Climatology*, 105, 263–275.
- Kouroutzoglou, J., Flocas, H.A., Keay, K., Simmonds, I. and Hatzaki, M. (2012) On the vertical structure of Mediterranean explosive cyclones. *Theoretical and Applied Climatology*, 110, 155–176.
- Kouroutzoglou, J., Flocas, H.A., Hatzaki, M., Keay, K. and Simmonds, I. (2013) A high-resolution climatological study on the comparison between surface explosive and ordinary cyclones in the Mediterranean. *Regional Environmental Change*, 14, 1833–1846.
- Kuwano-Yoshida, A. and Asuma, Y. (2008) Numerical study of explosively developing extratropical cyclones in the northwestern Pacific region. *Monthly Weather Review*, 136, 712–740.
- Lagouvardos, K., Kotroni, V. and Defer, E. (2007) The 21–22 January 2004 explosive cyclogenesis over the Aegean Sea: observations and model analysis. *Quarterly Journal of the Royal Meteorological Society*, 133, 1519–1531.
- Lee, J. G., Han, J. & Whang, K. Y. (2007) *Trajectory clustering: a partition-and-group framework*. Paper presented at the 2007 ACM SIGMOD International Conference on Management of Data, ACM, Beijing, China.
- Li, W., Xia, R., Sun, J., Fu, S., Jiang, L., Chen, B. and Tian, F. (2019) Layer-wise formation mechanisms of an entire-troposphere-thick extratropical cyclone that induces a record-breaking catastrophic rainstorm in Beijing. *Journal of Geophysical Research*, 124, 10567–10591.
- Lim, E.P. and Simmonds, I. (2002) Explosive cyclone development in the Southern Hemisphere and a comparison with Northern Hemisphere events. *Monthly Weather Review*, 130, 2188–2209.
- Lim, E.-P. and Simmonds, I. (2007) Southern hemisphere winter extratropical cyclone characteristics and vertical organization observed with the ERA-40 data in 1979–2001. *Journal of Climate*, 20, 2675–2690.
- Lorenz, E.N. (1955) Available potential energy and the maintenance of the general circulation. *Tellus*, 7, 157–167.
- Mann, H.B. and Whitney, D.R. (1947) On a test of whether one of two random variables is stochastically larger than the other. *Annals of Mathematical Statistics*, 18, 50–60.
- Martínez-Alvarado, O., Baker, L.H., Gray, S.L., Methven, J. and Plant, R.S. (2014) Distinguishing the Cold Conveyor Belt and Sting Jet Airstreams in an Intense Extratropical Cyclone. *Monthly Weather Review*, 142(8), 2571–2595.
- Messmer, M. and Simmonds, I. (2021) Global analysis of cyclone-induced compound precipitation and wind extreme events. *Weather and Climate Extremes*, 32, 100324.
- Murakami, S. (2011) Atmospheric local energetics and energy interactions between mean and Eddy fields. Part I: theory. *Journal of the Atmospheric Sciences*, 68, 760–768.
- Murty, T., Mcbean, G. and McKee, B. (1983) Explosive cyclogenesis over the northeast Pacific Ocean. *Monthly Weather Review*, 111, 1131–1135.
- Novak, D.R., Colle, B.A. and Aiyer, A. (2010) Evolution of meso-scale precipitation band environments within the comma head of northeast U.S. cyclones. *Monthly Weather Review*, 138, 2354–2374.
- Pang, H. and Fu, G. (2017) Case study of potential vorticity tower in three explosive cyclones over eastern Asia. *Journal of the Atmospheric Sciences*, 74, 1445–1454.

- Parton, G., Dore, A.J. and Vaughan, G. (2010) A climatology of mid-tropospheric mesoscale strong wind events as observed by the MST radar, Aberystwyth. *Meteorological Applications*, 17, 340–354.
- Pepler, A.S. and Dowdy, A.J. (2020) A three-dimensional perspective on extratropical cyclone impacts. *Journal of Climate*, 33, 5635–5649.
- Roeber, P.J. (1984) Statistical analysis and updated climatology of explosive cyclones. *Monthly Weather Review*, 112, 1577–1589.
- Rossa, A.M., Wernli, H. and Davies, H.C. (2000) Growth and decay of an extra-tropical cyclone's PV-tower. *Meteorology and Atmospheric Physics*, 73, 139–156.
- Rudeva, I. and Simmonds, I. (2015) Variability and trends of global atmospheric frontal activity and links with large-scale modes of variability. *Journal of Climate*, 28, 3311–3330.
- Sanders, F. (1987) Skill of NMC operational dynamical models in prediction of explosive cyclogenesis. *Weather and Forecasting*, 2, 322–336.
- Sanders, F. and Gyakum, J.R. (1980) Synoptic-dynamic climatology of the “bomb”. *Monthly Weather Review*, 108, 1589–1606.
- Schultz, D.M., Bosart, L.F., Colle, B.A., Davies, H.C., Dearden, C., Keyser, D., Martius, O., Roeber, P.J., Steenburgh, W.J. and Volkert, H. (2018) Extratropical cyclones: a century of research on meteorology's centerpiece. *Meteorological Monographs*, 59, 16.11–16.56.
- Simmonds, I. and Wu, X.R. (1993) Cyclone behavior response to changes in winter Southern-Hemisphere sea-ice concentration. *Quarterly Journal of the Royal Meteorological Society*, 119, 1121–1148.
- Simmonds, I. (2000) Size changes over the life of sea level cyclones in the NCEP reanalysis. *Monthly Weather Review*, 128, 4118–4125.
- Sinclair, M.R. (1994) An objective cyclone climatology for the Southern Hemisphere. *Monthly Weather Review*, 122, 2239–2256.
- Tilinina, N., Gulev, S.K., Rudeva, I. and Koltermann, P. (2013) Comparing cyclone life cycle characteristics and their inter-annual variability in different reanalyses. *Journal of Climate*, 26, 6419–6438.
- Uccellini, L.W., Keyser, D., Brill, K.F. and Wash, C.H. (1985) The Presidents' Day Cyclone of 18–19 February 1979: influence of upstream trough amplification and associated tropopause folding on rapid cyclogenesis. *Monthly Weather Review*, 113, 962–988.
- Ulbrich, U., Leckebusch, G.C., Grieger, J., Schuster, M., Akperov, M., Bardin, M.Y., Feng, Y., Gulev, S., Inatsu, M., Keay, K., Kew, S.F., Liberato, M.L.R., Lionello, P., Mokhov, I.I., Neu, U., Pinto, J.G., Raible, C.C., Reale, M., Rudeva, I., Simmonds, I., Tilinina, N.D., Trigo, I.F., Ulbrich, S., Wang, X., Wernli, H. and Team, I. (2013) Are greenhouse gas signals of Northern Hemisphere winter extra-tropical cyclone activity dependent on the identification and tracking algorithm? *Meteorologische Zeitschrift*, 22, 61–68.
- Yamamoto, M. (2012) Rapid merger and recyclogenesis of twin extratropical cyclones leading to heavy precipitation around Japan on 9–10 October 2001. *Meteorological Applications*, 19, 36–53.
- Yoshida, A. and Asuma, Y. (2004) Structures and environment of explosively developing extratropical cyclones in the northwestern Pacific region. *Monthly Weather Review*, 132, 1121–1142.
- Zhang, S.Q., Fu, G., Lu, C.G. and Liu, J.W. (2017) Characteristics of explosive cyclones over the Northern Pacific. *Journal of Applied Meteorology and Climatology*, 56, 3187–3210.

How to cite this article: Jiang, L.-Z., Fu, S.-M., Sun, J.-H., Fu, R., Li, W.-L., Zhao, S.-X., & Wang, H. (2021). Surface wind and vertical extent features of the explosive cyclones in the Northern Hemisphere based on the ERA-I reanalysis data. *International Journal of Climatology*, 1–22. <https://doi.org/10.1002/joc.7284>